A unified model for the dynamics of ATP-independent ultrafast contraction

Carlos Floyd,[1] Arthur T. Molines,[2] Xiangting Lei,[3] Jerry E. Honts,[4] Fred Chang,[2] Mary Williard Elting,[5, a)] Suriyanarayanan Vaikuntanathan,[1, b)] Aaron R. Dinner,[1, c)] and M. Saad Bhamla[3, d)]

[1)] *Department of Chemistry and James Franck Institute, University of Chicago, Chicago, IL 60637*

[2)] *Department of Cell and Tissue Biology, University of California, San Francisco, CA 94143*

[3)] *School of Chemical and Biomolecular Engineering, Georgia Institute of Technology, Atlanta, GA 30318*

[4)] *Department of Biology, Drake University, Des Moines, IA 50311*

[5)] *Department of Physics, North Carolina State University, Raleigh, NC 27607*

In nature, several ciliated protists share the remarkable ability to undergo ultrafast motions using protein assemblies called myonemes, which contract in response to Ca^{2+} ions. These systems are not adequately described by existing theories, such as those of actomyosin contractility and macroscopic biomechanical latches, and new models are needed to understand their mechanism. Here, we image and quantitatively analyze the contractile kinematics observed in two ciliated protists (*Vorticella sp* and *Spirostomum sp*), and, based on mechanochemistry of the organisms, we introduce a minimal mathematical model that reproduces our and published observations. Analysis of the model reveals a set of three dynamic regimes, which are differentiated by the rate of chemical driving and the importance of inertia. We describe their distinct scaling behaviors and kinematic signatures. In addition to providing insight into Ca^{2+}-powered myoneme contraction in protists, our work can guide the rational design of ultrafast bioengineered systems such as active synthetic cells.

I. INTRODUCTION

A well-known molecular mechanism for motion in biological systems is actomyosin contractility, which involves the relative sliding of actin filaments due to ATP hydrolysis by bound molecular motors[1]. However, the fastest motions currently known to occur in the biological world (measured as the proportional change in length per unit time) are due not to actomyosin assemblies but to lesser-known protein assemblies called myonemes[2–4]. We use "myonemes" in the broadest sense[5], encompassing terms used for specific organisms such as "spasmonemes" and "M-bands." Myonemes are common in ciliated protists: for example, they are found in the wine glass-shaped genus *Vorticella*[6,7], the cigar-shaped genus *Spirostomum*[8–10], and the chandelier-shaped genus *Zoothamnium*[11,12]. Similar Ca^{2+}-responsive supramolecular assemblies are proposed to occur in a range of other single-celled organisms[13–20], and possibly even plants[21–23]. The mechanism of ultrafast myoneme contraction is qualitatively different from actomyosin contraction in that ATP is not directly consumed during the contractile motion[6,24]. Instead, a local increase in Ca^{2+} concentration acts as a mechanical actuator to initiate contraction[25–28]. ATP is subsequently consumed to pump Ca^{2+} away from the myoneme fibers and reset the process[11,29].

While several experimental studies have been conducted on myoneme-based contraction dynamics[7–11,30–38], it is difficult to draw general conclusions without a theoretical framework to interpret the observations. Whereas actomyosin contractility has been extensively studied theoretically and computationally[39–44], Ca^{2+}-powered myoneme-based contractility is relatively unexplored from a modeling point of view. An existing computational model of *Vorticella*[45] is specific to the geometry of the organism and thus does not apply across species. Previous mechanochemical analyses also do not address the dynamics of contraction[6,9]. Open questions that a mathematical model of myoneme contraction might address are: what synchronizes contraction across the organism's length, what sets the rate of chemical driving, and what are the key geometric and mechanical factors (such as the organism's dimensions and environmental viscosity) that affect the contraction dynamics?

Here, we develop a minimal mathematical model of myoneme contraction and show that it applies across species. In our model, an elastic medium in a dissipative environment is driven out of equilibrium by a traveling wave of shrinking rest lengths, which captures the effect of a traveling Ca^{2+} wave. This simple setup omits several system-specific details but can fit experimental contraction measurements for *Spirostomum* and *Vorticella*. Mathematically, the model comprises a wave equation with dissipation and a non-autonomous source term. We derive an approximate form for the non-autonomous function by analyzing an auxiliary kinetic model for a traveling Ca^{2+} wave. Using the model, we show that the balance between chemical driving, mechanical stiffness, and viscous drag results in three dynamic regimes. These regimes are distinguished by the relative importance of inertia and Ca^{2+} wave speed, and they exhibit kinematic signatures, including asymmetric contraction

[a)] Electronic mail: mary.elting@ncsu.edu
[b)] Electronic mail: svaikunt@uchicago.edu
[c)] Electronic mail: dinner@uchicago.edu
[d)] Electronic mail: saadb@chbe.gatech.edu

and different scaling behavior of the maximum contraction velocity. This work provides a starting point for extracting general mechanochemical principles of myoneme contraction in biological and engineered systems.

II. MODEL DERIVATION

Myoneme contraction is driven by an increase in cytosolic Ca^{2+}, which occurs as a traveling wave that traverses the organism's length in several milliseconds[26,45–48]. The mechanism by which Ca^{2+} physically induces contraction is believed to be a screened entropic spring effect: Ca^{2+} binds to the negatively charged myoneme fibers and screens their electrostatic self-repulsion, which allows for the entropic contribution to the free energy to favor collapse of the polymer[49]. This system is sometimes considered a polyelectrolyte gel, in which thermodynamic balances of entropic and osmotic forces determine the gel's equilibrium[11,50,51]. The precise contributions to the myoneme free energy as a function of length are not needed to formulate a minimal mechanical model, and we make the phenomenological assumption that the system obeys linear elasticity[52]. The key difference from the usual elastic theory is that the rest lengths of the elastic elements are dynamic quantities that depend on the local concentration of bound Ca^{2+} (Figure 1). We study here a one-dimensional model and neglect any contributions from orthogonal dimensions and twisting effects which, in the real system, may alter the one-dimensional dynamics through elastic couplings[53,54]. As elaborated in *Appendix Supplementary methods* Section B 2, we assume that these coupling coefficients are negligible to a first approximation.

To formulate the model mathematically, we start from a discrete chain of harmonic springs in one dimension with externally imposed rest lengths, and we define $X_i(T)$ as the position of the ith mass at time T. The spring stiffness parameter k, mass m, drag γ, and initial rest length δ, are the same for all springs, and the instantaneous rest length $G_{i+\frac{1}{2}}(T)$ of the spring connecting masses i and $i+1$ is a non-autonomous function which we specify later. The force on mass i is

$$m\partial_T^2 X_i = k\left(X_{i+1} - X_i - G_{i+\frac{1}{2}}\right) - k\left(X_i - X_{i-1} - G_{i-\frac{1}{2}}\right) - \gamma\partial_T X_i. \quad (1)$$

Rather than a discrete description in terms of the index i, we seek a continuum description of the dynamics in terms of a material coordinate $S \in [0, L]$, where L is the uncontracted length of the system. By Taylor expanding the functions X and $g \equiv G/\delta$ to second order in δ and then letting $\delta \to 0$, we find the following partial differential equation (PDE) for the position $X(S,T)$:

$$\partial_T^2 X - \alpha\left(\partial_S^2 X - \partial_S g\right) + \mu\partial_T X = 0. \quad (2)$$

Here, $\alpha = k\delta^2/m = EA/\rho$ is the product of the Young's modulus E and the effective spring cross-sectional area A divided by the linear mass density $\rho = m/\delta$ (where we used $k = EA/\delta$[52]). The parameter α can be interpreted as the square of the speed of sound in the spring chain[55]. $\mu = \gamma/(\delta\rho)$ is the ratio of the drag constant per unit length to the mass density, and $g(S,T)$ is a non-autonomous function for the local "target" strain, defined as the ratio of the current spring rest length $G(S,T)$ to the initial rest length δ. The quantities g, α, and μ remain finite as $\delta \to 0$ because $G \sim \delta$, $k \sim \delta^{-1}$, $m \sim \delta$ and $\gamma \sim \delta$, while E, A, and ρ are independent of δ. Eq. (2) represents the force balance of $X(S,T)$, where the first term is the acceleration, the second term (proportional to α) captures the force due to the difference between the local strain and the target strain g, and the third term captures the drag force. See *Appendix Supplementary methods* Section B 1 for further details of the derivation of the model.

We find the boundary conditions by retaking the continuum limit at the terminal masses in the discrete representation (Eq. (1)), noting that these masses are connected to only a single spring. This yields

$$\partial_S X(S,T) = g(S,T) \text{ at } S = 0,\ L. \quad (3)$$

In the case of *Vorticella*, which has one end (say $S = L$) attached to a fixed substrate, we use the boundary condition $X(L,T) = L$ at that end. We further take the initial conditions

$$X(S,0) = S \text{ and } \partial_T X(S,0) = 0. \quad (4)$$

We discuss this model's physical justification and limitations in *Appendix Supplementary methods* Section B 2.

We model the target strain $g(S,T)$ as a linear function of the local concentration of Ca^{2+} bound to the myoneme fibers; see Eq. (17). Specifying the target strain function $g(S,T)$ requires describing the Ca^{2+} dynamics, for which we adapt a tractable reaction-diffusion model of a traveling Ca^{2+} wave[56], as described in *Materials and methods* Section V A. By analyzing this model, we found that a good approximation to the target strain function $g(S,T) = g^*(S - VT; W)$ is a traveling wave moving at speed V and having a sigmoidal profile g^* with width W (Eq. (22)). The function decreases from 1 to $g_{\min} \in [0,1]$ as the wave passes through the organism. An additional parameter O sets the time offset such that the center of the wave arrives at $S = 0$ at time O. As described in *Results* Section III B, we can approximately express V and W in terms of the kinetic parameters of the Ca^{2+} model (Eq. (5) and Eq. (B31)).

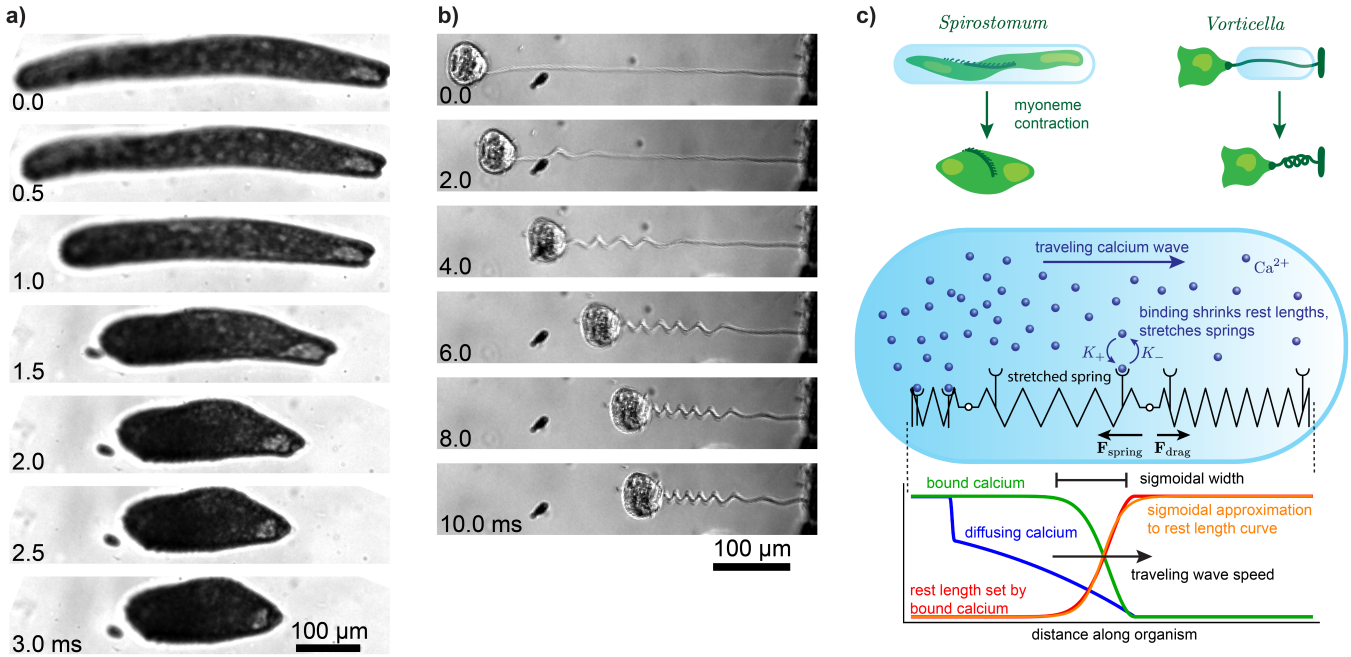

FIG. 1. **Myoneme-based contraction in ciliated protists.** (a) Images of *Spirostomum* undergoing contraction, with the time in milliseconds labeled on the bottom right of each image. Rapid contraction begins at $T = 0$ ms and is followed by a slower re-elongation phase (not shown). Note that the left side of the organism begins contracting (between 0.5 and 1.0 ms) before the right (between 1.0 and 1.5 ms). (b) Same as (a) for *Vorticella*. (c) Schematic of the model. The contractile body of *Spirostomum* and stalk of *Vorticella* are abstracted as a 1D elastic medium in a viscous environment, represented as a chain of springs. The local spring rest length (depicted as the number of ridges) depends on the number of bound Ca^{2+} ions (shown as blue spheres bound to receptors on the spring). A rightward traveling Ca^{2+} wave thus shrinks the spring rest lengths, exerting forces in the chain which then contracts against viscous drag. The bottom graph schematically illustrates several quantities in our mechanochemical model at a fixed time, which we elaborate on in the main text.

III. RESULTS

A. A minimal continuum model reproduces contraction kinematics

Despite the model's simplicity, we find that it reproduces the contraction kinematics of *Spirostomum* and *Vorticella* semi-quantitatively. We illustrate this by comparing the trajectories of normalized length $\lambda(T) \equiv (X(L,T) - X(0,T))/L$ from experimental measurements to fitted model curves. Contraction events for *Spirostomum* and *Vorticella* are shown in *Appendix Supplementary movies* S1 and S2, and see *Materials and methods* Section V C for a description of the experimental methods. The second-order non-autonomous PDE model does not have an exact closed form solution, though we describe exact series solutions in two limiting cases in *Results* Section III C. To fit the model, we numerically integrate the PDE with different choices of parameters and compare the results to the experimental traces. In Figure 2a, we show five contraction measurements in *Spirostomum* along with a model solution fitted to their average, illustrating the feasibility of our model in capturing the contraction dynamics. The corresponding contraction velocities $|\partial_T \lambda|$ are shown in Figure 2b. We also fit the model with a fixed boundary condition at $S = L$ to data for five *Vorticella* contraction events (Figures 2c,d).

In *Appendix* Figures 9 and 10, we display fits to each of the five individual trajectories in Figure 2, showing that excellent fits can be obtained for all trajectories using fairly consistent parameters. A typical set of parameters for *Spirostomum* from these individual fits is $L = 0.58$ mm, $g_{\min} = 0.35$, $\mu/\alpha = 28$ ms/mm^2, $V = 0.8$ mm/ms, and $W = 0.12$ mm. For *Vorticella*, typical set of parameters is $L = 0.24$ mm, $g_{\min} = 0.18$, $\mu/\alpha = 40$ ms/mm^2, $V = 0.13$ mm/ms, and $W = 0.04$ mm. The value of α is fixed at 1 for all trajectories because, as explained more in *Results* Section III C, in this regime, the dynamics are approximately determined only by the ratio μ/α. In *Appendix Supplementary results* Section A 2 we show that the fitted parameters for *Vorticella* are consistent in order of magnitude with physiological parameters used for a detailed computational model in Ref. 45. The quantity μ/α has large variations between the fitted trajectories, and according to a two-tailed t-test, the two organisms do not have significantly different values. This implies that the individual-to-individual drag and elasticity variability is comparable to the between-species variability. However, V and W values are more closely grouped for each organism, and the means of these

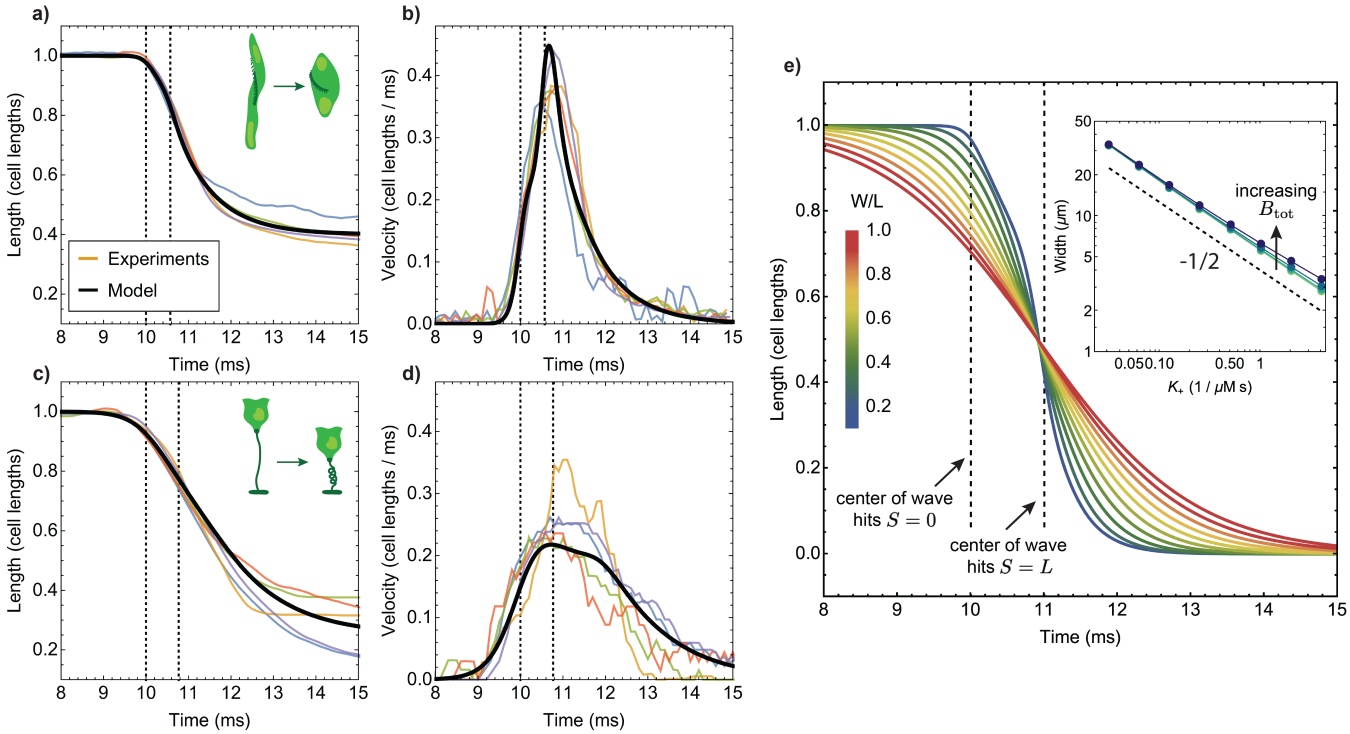

FIG. 2. **Comparison of the model to experimental data.** (a) Five measurements of *Spirostomum* contraction, collapsed to the same scale by normalizing length using the organism's uncontracted length L and by offsetting time so that contraction begins around $T = 10$ ms. The black curve shows the model fit to all of these trajectories at once; see *Appendix Supplementary results* Section A 2 for fits to the individual curves. Vertical dashed lines indicate the times in the model solution when the center of the target strain wave arrives at $S = 0$ and $S = L$. Time is shifted by choosing $O = 10$ ms in Eq. (22) to achieve numerical agreement between the boundary and initial conditions (see *Material and methods* Section V B). (b) The corresponding velocity trajectories, obtained by numerically differentiating the data in (a). (c) and (d) The same as (a) and (b) but for *Vorticella* contraction. (e) Simulated length trajectories with $V = 1$ L/ms, $\alpha = 2$ $(L/\text{ms})^2$, $g_{\min} = 0$, $O = 10$ ms, and $\mu = 10$ ms^{-1}. The width W of the wave is varied from 0.1 L to 1.0 L in steps of 0.1L as the colors range from blue to red. The inset shows how W depends on the binding rate K_+ in the Ca^{2+} model. The total myoneme concentration $B_{\rm tot}$ ranges from 500 to 4,000 μM in multiples of 2 as the colors range from light green to purple. The dashed line in the inset represents the analytically predicted scaling $W \sim K_+^{-1/2}$. For the remaining parameters used in the inset, see *Appendix Supplementary methods* Section B 3.

parameters are statistically different for the two organisms (t-test p-value $\ll 0.05$). We explore V and W more next.

B. Ca^{2+} dynamics control contraction

How rapidly the length changes in time depends on the speed V and, less intuitively, the width W of the target strain wave $g(S - VT; W)$. As W decreases, the target strain wave approaches a traveling step function in which the springs ahead of the wave have their original rest lengths and those behind have rest lengths $g_{\min}$. As W increases, the distribution of changing rest lengths is wider, and the driving and relaxation are more spatially and temporally homogeneous. We illustrate this in Figure 2e, where the length trajectory is shown for several values of W.

Since the parameters V and W control the length and velocity trajectories, it is interesting to understand which features of the Ca^{2+} dynamics control these parameters. For this, we analyzed the Ca^{2+} model, which was previously shown to obey the approximate relationship[56]

$$V \approx \sqrt{\frac{JD_C}{C_0}}, \tag{5}$$

where J is the Ca^{2+} influx of open channels, D_C is the diffusion constant of Ca^{2+}, and C_0 is the concentration threshold of the Ca^{2+} channels (see *Materials and methods* Section V A and *Appendix Supplementary methods* Section B 3 for more details). We added binding of Ca^{2+} to myoneme fibers to the model and derived a new relationship for the width W:

$$W \approx \sqrt{\frac{D_C}{K_+ C_0}}, \tag{6}$$

where K_+ is the rate that Ca^{2+} binds to myonemes. Nu-

merical confirmation of this relationship is illustrated in *Appendix Supplementary methods* Section B 3 and the inset of Figure 2e. A seemingly restrictive assumption made in the derivation of Eq. (B31) is that the total concentration of myoneme binding sites B_{tot} is much smaller than the typical cytosolic Ca^{2+} concentration. However, we find numerically that the predicted scaling holds even as B_{tot} is increased to relatively large values.

The result of this analysis is that features in the dynamics of contraction (like the time it takes the length to change) can inform us about the magnitudes of the underlying biophysical parameters (like the binding rate K_+). Assuming that D_C is the same in both organisms (although this could be affected by the presence of internal buffers[56]), the values of V and W estimated for *Vorticella* and *Spirostomum* imply via Eqs. (5) and (B31) that these organisms have different threshold Ca^{2+} concentrations C_0[26,57,58] and different release rates J or binding constants K_+. This minimal model thus takes a first step toward connecting contraction dynamics and the organisms' biochemistry, but more *in vivo* experiments are needed to test these predictions.

C. Dimensional analysis reveals the minimal set of model parameters

The model considered so far (Eq. (2) together with Eq. (22)) is written in dimensional quantities and depends on the parameters α and μ, which are related to the stiffness of the material and viscosity of the environment, and V, W, and $g_{\min}$, which are the speed, width, and minimum value of the target strain wave. However, these parameters are not all independent. For example, rescaling time or space by a common factor would leave the dynamics unchanged. We now show that it is possible to reduce the number of parameters by one through non-dimensionalization. We use lowercase variables throughout to denote dimensionless quantities.

There are two length scales, W and L, and we pick the uncontracted length L as the reference length and define $s = S/L$, $x = X/L$, and $w = W/L$. Next, three time scales can be defined:

$$\tau_w = \frac{L}{V},\ \tau_m = \frac{L}{\sqrt{\alpha}},\ \text{and}\ \tau_d = \frac{1}{\mu}. \tag{7}$$

Here, τ_w is the wave time scale, which represents the time taken for the center of the traveling wave to traverse the length L; τ_m is the material time scale, which represents the time taken for a sound wave to traverse the length of the spring chain; τ_d is the drag time scale, characterizing the exponential deceleration of motion due to viscous damping. We non-dimensionalize time using $t = T/\tau_w$. In these units, the wave speed is equal to 1, and Eq. (2) is expressed as the following PDE for $x(s,t)$:

$$\partial_t^2 x - \eta_{w,m}^2 \left(\partial_s^2 x - \partial_s f^*(s-t)\right) + \eta_{w,d}\partial_t x = 0, \tag{8}$$

where $f^*(y) \equiv g^*(Ly)$ is the target strain wave profile, rewritten to take a dimensionless argument y. The size of τ_w relative to the two remaining time scales defines the non-dimensional parameters

$$\eta_{w,m} \equiv \frac{\tau_w}{\tau_m} = \frac{\sqrt{\alpha}}{V}\ \text{and}\ \eta_{w,d} \equiv \frac{\tau_w}{\tau_d} = \frac{\mu L}{V}. \tag{9}$$

The parameter $\eta_{w,m}$ describes the ratio of the myonemal speed of sound (which depends on the stiffness and density) to the wave traversal speed and is independent of length. The parameter $\eta_{w,d}$ describes the ratio of the drag time scale (depending on viscosity and density) to the wave traversal speed and is proportional to the length.

We can further simplify these non-dimensional dynamics by taking the "slow wave" limit $\eta_{w,m},\ \eta_{w,d} \gg 1$, in which Eq. (8) reduces to

$$\partial_t x - \zeta\left(\partial_s^2 x - \partial_s f^*(s-t)\right) = 0, \tag{10}$$

where the only remaining parameter is

$$\zeta \equiv \frac{\tau_d \tau_w}{\tau_m^2} = \frac{\alpha}{V\mu L}. \tag{11}$$

Eq. (10) can be viewed as an over-damped limit of the model, in which inertia has dropped out of the dynamics because only a first derivative with respect to time remains, and in which mass is no longer relevant because ζ is independent of ρ.

Eq. (10) is similar to the diffusion (or heat) equation with a source term. One difference is the boundary conditions: typically, the heat equation has fixed Dirichlet or Neumann boundary conditions, yet x obeys a boundary condition that depends in time on $f^*(s-t)$ (cf. Eq. (3)). However, we can define

$$h(s,t) = \partial_s x(s,t) - f^*(s-t), \tag{12}$$

and express Eq. (10) as

$$\partial_t h - \zeta\partial_s^2 h = -\partial_t f^*(s-t). \tag{13}$$

The boundary conditions are now the fixed Dirichlet conditions $h(0,t) = h(1,t) = 0$, and thus Eq. (13) is exactly the diffusion equation with a source term $-\partial_t f$, for which exact series solutions can be found. The mixed boundary conditions of *Vorticella* also result in mixed boundary conditions for the diffusion equation.

We also consider a "quench" limit $\eta_{w,d},\ \eta_{m,d} \ll 1$, in which the traveling wave moves at infinite speed, such that the rest lengths of all the springs are set to their new values before the organism can react. This implies that $f(s,t) = f(s)$ is independent of time. The dynamics consist of only the subsequent relaxation of the system to its equilibrium

$$x^{\text{eq}}(s) = \int_0^s f(s')ds' + \text{constant}, \tag{14}$$

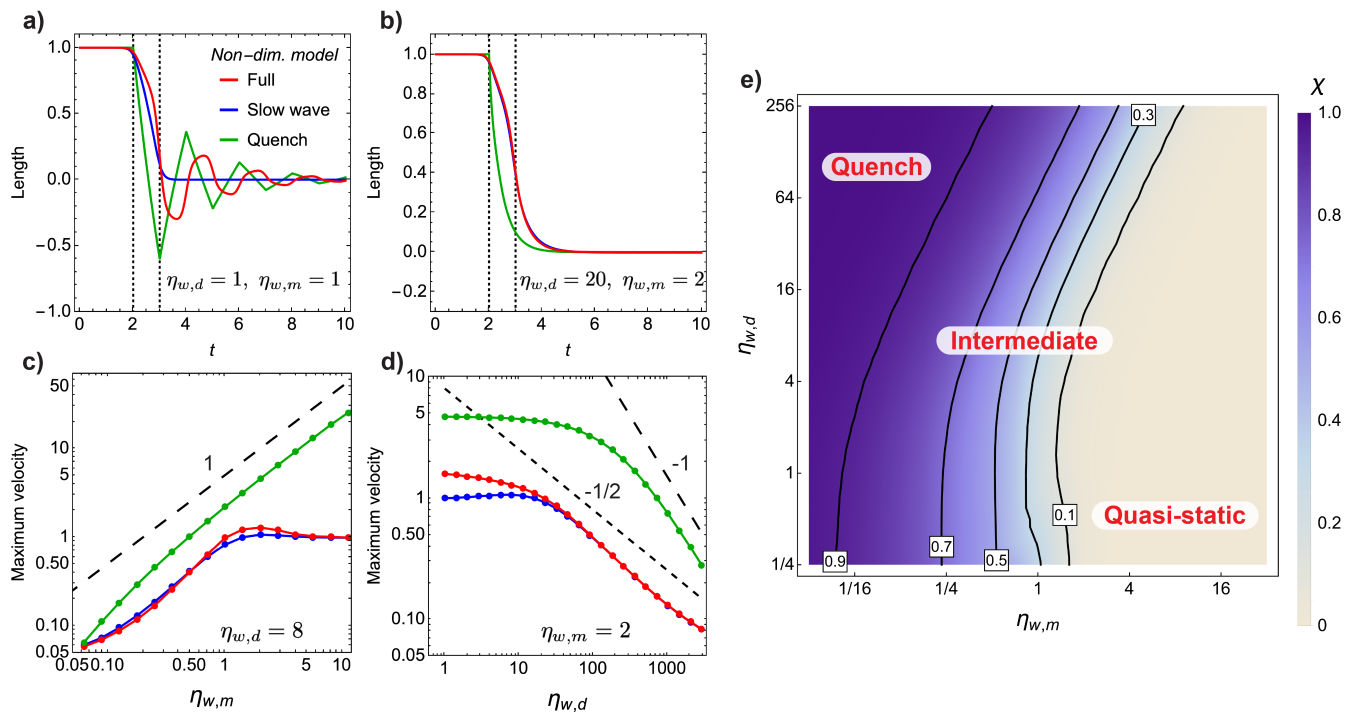

FIG. 3. **The non-dimensional model and its limiting versions capture key kinematic properties of contraction**. (a) Non-dimensional length $\lambda(t)$ as a function of time for the three versions of the non-dimensional model. Parameter values are $\eta_{w,d} = \eta_{w,d} = 1,\ w = 0.1,\ g_{\min} = 0$. The vertical lines at $t = 2$ and 3 indicate the times when the center of the target strain wave enters and exits the system. For the quench model, the quench occurs at $t = 2$. (b) Same as (a) but with $\eta_{w,d} = 2$ and $\eta_{w,d} = 20$. (c) and (d) Scaling of $\dot{\lambda}_{\max}$ with $\eta_{w,m}$ (c) and $\eta_{w,d}$ (d) for the three models. The colors are the same as in (a). For panel (c), $\eta_{w,d}$ is fixed at 8, while for panel (d), $\eta_{w,m}$ is fixed at 2. (e) Heatmap of χ, the peak elastic energy stored in the system as a fraction of the maximum possible energy, as $\eta_{w,m}$ and $\eta_{w,d}$ are varied for the full model. Contours are drawn and labeled at selected values of χ.

where the constant may be set to zero. The deviation from equilibrium, $y(s,t) \equiv x(s,t) - x^{\mathrm{eq}}(s)$, obeys the dynamics

$$\partial_t^2 y(s,t) - \partial_s^2 y(s,t) + \eta_{m,d}\partial_t y(s,t) = 0 \qquad (15)$$

with the initial condition $y(s,0)) \equiv x(s,0) - x^{\mathrm{eq}}$, $\partial_t y(s,0) = 0$, and open boundary conditions $\partial_s y(0,t) = \partial_s y(1,t) = 0$. We note that the one remaining parameter

$$\eta_{m,d} \equiv \frac{\tau_m}{\tau_d} = \frac{\mu\sqrt{\alpha}}{L} \qquad (16)$$

is independent of wave speed, which is infinite. The quench limit has an exact Fourier series solution, described in *Appendix Supplementary methods* Section B 4.

In Figures 3a and b we compare the solutions of the full non-dimensional model (Eq. (8)), the slow wave model (Eq. (10)), and the quench model (Eq. (15)) for two sets of the non-dimensional parameters $\eta_{w,d}$ and $\eta_{m,d}$. In these plots we fix $w = 0.1$ and $g_{\min} = 0$ for simplicity. For $\eta_{w,d} = \eta_{m,d} = 1$ (Figure 3a), the models all behave quite differently because neither limiting case is reached. Decaying oscillations about $l = 0$ are observed for the full and quench model, while the slow wave model does not oscillate because it lacks inertia. The oscillations for the quench and full model have the same frequency (which is proportional to $\eta_{m,d}$, reflecting the resonant frequency of the spring chain) yet different waveforms and amplitudes. For $\eta_{w,d} = 20,\ \eta_{m,d} = 2$ (Figure 3b), the full model and slow wave model are in close agreement.

A stark feature of the full model compared to the quench model is the asymmetry of contraction: in the quench model, all springs instantly have new rest lengths, so all springs relax simultaneously and symmetrically about the center $s = 0.5$. This is not the case for the full model, where the wave first arrives at $s = 0$, causing the springs to begin relaxing before those at $s = 1$. This asymmetry of contraction can be observed in the experimental images of *Spirostomum* and *Vorticella* in Figures 1a and b, and we further illustrate this in Figure 4a,b,c. In Figure 4d,e,f,g we show $x(s,t)$ at several values of t for the full and quench models corresponding to the length trajectories shown in Figures 3a and b.

From the fits to the experimental data of *Vorticella* and *Spirostomum* contracting in water (see *Appendix Supplementary results* Section A 2), neither organism is expected to obey the quench-like dynamics, being closer to

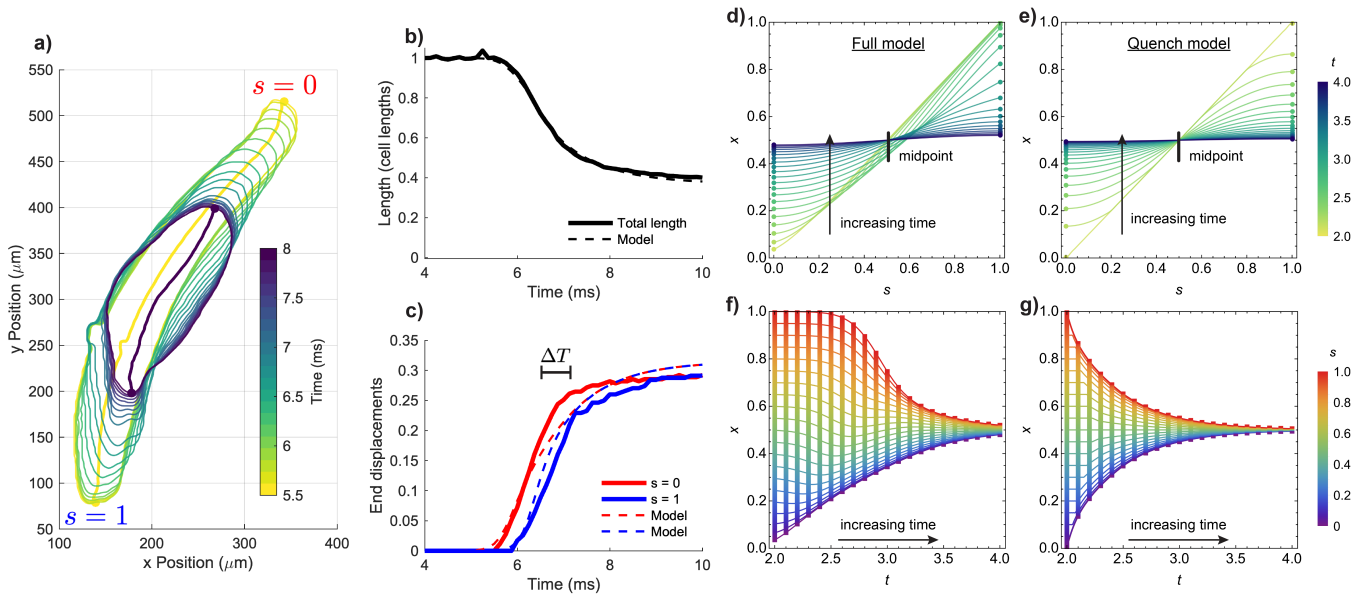

FIG. 4. **Asymmetric contraction of *Spirostomum*.** (a) A sequence of contours of *Spirostomum* obtained from 8,000 Hz video imaging. Colors range from yellow to purple as time ranges from 5.5 ms to 8 ms. The initial and final midlines, whose arc lengths determine the measured length of the organism, are drawn in yellow and purple. (b) The trajectory of the length during this contraction event. The dashed curved shows the trajectory of the simulated model, which was fit to match the experimentally measured solid curve. (c) The displacement trajectories of the top (red) and bottom (blue) ends of the midlines and the corresponding quantities in the fitted model are shown as dashed curves. These displacements were measured by projecting the endpoints to the initial midline curve and computing the arc length from the end to the projected point. Asymmetric contraction can be observed as the top end begins contracting before the bottom end (by a time difference labeled ΔT), a feature that the fitted model semi-quantitatively reproduces. (d) and (e) Corresponding to Figures 3a,b the entire $x(s,t)$ curves for the full and quench models. The colors in these panels range from yellow to blue as t increases from 2 to 4 in steps of 0.1. Panels (f) and (g) show the same curves as a function of t, rather than s.

the slow-wave limit. This implies that the organisms are relaxing appreciably *while* the Ca^{2+} wave traverses their lengths.

D. Scaling behavior distinguishes three dynamic regimes

An additional significant difference between the different models is the scaling of the maximum contraction velocity with the viscosity. Notably, this has been studied in previous experimental and computational works on *Vorticella* and *Spirostomum*, against which we may validate our model[9,38,45].

To explore this scaling behavior, we computed the maximum velocity $\dot{\lambda}_{\max} \equiv \max_t |\partial_t \lambda(t)|$ as we varied the non-dimensional parameters $\eta_{w,m}$ and $\eta_{w,d}$ in the full, quench, and slow wave models. The results are displayed in Figure 3c and d, again setting $w = 0.1$ and $g_{\min} = 0$ for simplicity. The dynamics of the quench model only depend on the dimensionless parameter $\eta_{m,d}$ (cf. Eq. (15)), and the maximum velocity asymptotically scales like $\dot{\lambda}_{\max} \sim \eta_{m,d}^{-1} = \eta_{w,m}/\eta_{w,d} = L/\mu\sqrt{\alpha}$. This can be qualitatively understood as follows: as shown in *Appendix Supplementary methods* Section B 4, an exact solution for the quench model can be constructed by decomposing the initial condition into spatial Fourier modes and solving for the decay of each mode. Each mode acts like a mass, attached to a wall by a stretched spring with an effective drag constant $\eta_{m,d}$, which is suddenly released (see *Appendix* Eq. (B41)). By Stokes' law, the maximum velocity should then scale inversely with $\eta_{m,d}$ as observed.

For both the full and slow wave models, $\dot{\lambda}_{\max} \sim \eta_{w,m}$ up to a point at which $\dot{\lambda}_{\max}$ plateaus at 1. This results from the contraction speed not significantly exceeding the speed of the traveling target strain wave, which is defined as 1 in these units. Interestingly, for both models $\dot{\lambda}_{\max}$ asymptotically scales like $\dot{\lambda}_{\max} \sim \eta_{w,d}^{-1/2}$. To understand this, recall that the slow wave model can be formally mapped to the diffusion equation with a source term (cf. Eq. (10) and Eq. (13)). The dynamics are thus characterized by the "diffusion constant" $\zeta = \eta_{w,m}^2/\eta_{w,d} = \alpha/V\mu L$. For diffusion, it is known that an initial perturbation to the system spreads out over time with a length scale that grows like $\sqrt{\zeta t}$, which implies that the corresponding velocity scales like $\zeta^{1/2}$. This fact explains both the observed scaling $\dot{\lambda}_{\max} \sim \eta_{w,m}$ up to its saturation at 1, and the asymptotic scaling $\dot{\lambda}_{\max} \sim \eta_{w,d}^{-1/2}$. We emphasize that in Figure 3, we have assumed the wave width $W = 0.1\ L$; as demonstrated in *Appendix* Figure 7, different scaling behaviors result if

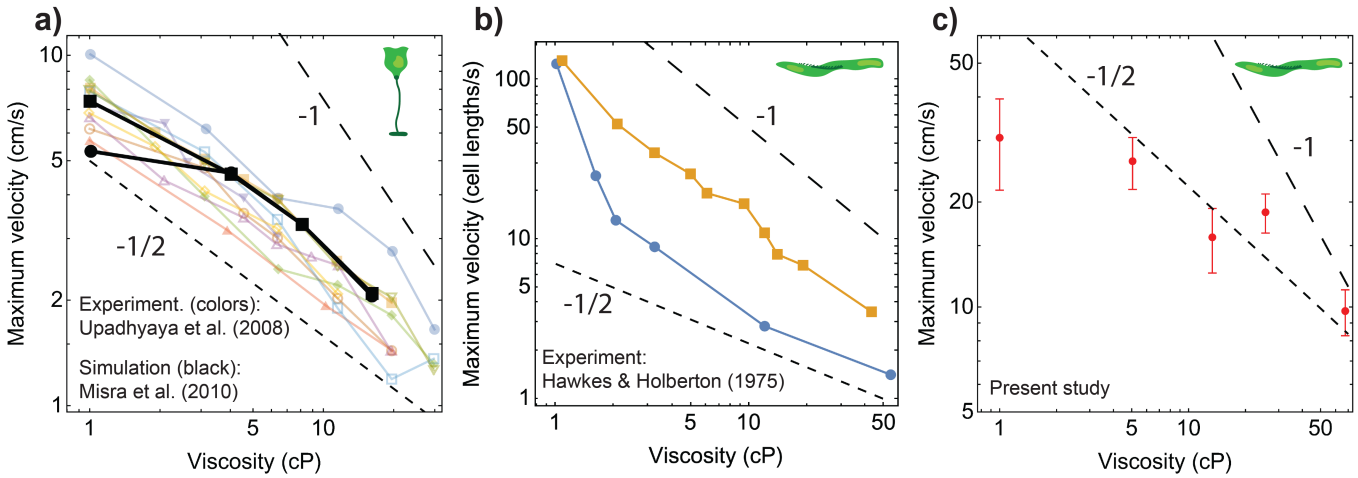

FIG. 5. **Experimentally measured velocity scaling**. (a) Published data on the maximum contraction velocity of *Vorticella* in solutions of different viscosities. Each colored line represents a single cell exposed to varying viscosities; these data are from Figure 3b of Ref. 38. The black points represent results from computational simulations, from Figure 4a in Ref. 45. The circle and square represent two values of Young's modulus. (b) Published data from Figure 2 of Ref. 9 on the maximum contraction velocity of *Spirostomum* in different viscosities and confinement methods: orange represents a setup using plane parallel glass surfaces and blue represents a setup using a narrow agar channel. Each point represents an average of 10-23 measurements, and connecting lines are drawn to guide the eye. (c) Measurements of the maximum contraction velocity of free-swimming *Spirostomum* in solutions of different viscosities. The mean and standard deviation over $5-10$ measurements for each viscosity condition are displayed. The published data were extracted from Refs. 38, 45, and 9 using WebPlotDigitizer[59].

one varies the uncontracted length L while holding the width W fixed rather than letting W change with L.

In Refs. 38 and 45 the scaling of $\dot{\lambda}_{\max}$ with the solution viscosity ν for *Vorticella* is measured to be $\dot{\lambda}_{\max} \sim \nu^{-1/2}$. This is consistent with our observed scaling $\dot{\lambda}_{\max} \sim \zeta^{1/2}$ for the full and slow wave models when holding all other parameters constant and only varying μ (which is proportional to ν). Our model thus exhibits the scaling observed in existing experimental data for *Vorticella*. We note that an alternate description for the $\nu^{-1/2}$ scaling based on power-limited contraction was provided in Ref. 38. Our explanation here does not involve a physical assumption about power conservation and follows solely from the dynamical equations.

Data for *Spirostomum* are available in Refs. 8 and 9 (Figure 5b). In these experiments, to aid imaging, the cells are confined in either a narrow agar channel (blue points) or between a microscope slide and a glass coverslip (orange points). Depending on the confinement method, the scaling appears consistent with either $\dot{\lambda}_{\max} \sim \nu^{-1}$, corresponding to the quench regime, or $\dot{\lambda}_{\max} \sim \nu^{-1/2}$. Our fits in Figure 2, together with observation of the asymmetric contraction dynamics (Figure 5a), suggest that *Spirostomum* should not be in the quench regime. The quench-like scaling may be an artifact of confinement, which could prevent the organism from contracting during the traversal of the wave, effectively quenching the springs. The imaging rate in Refs. 8 and 9 (800 Hz) may also be too low to resolve the maximum in the velocity profile precisely. We thus performed our measurements of the contraction of free-swimming *Spirostomum* using a high-speed camera, recording at a minimum of 2,000 Hz. The results, displayed in Figure 5c, are consistent with the predicted scaling $\dot{\lambda}_{\max} \sim \nu^{-1/2}$, though we cannot conclusively exclude the scaling $\dot{\lambda}_{\max} \sim \nu^{-1}$. We note that the low $\dot{\lambda}_{\max}$ at 1 cP is consistent with the predicted roll-off at low viscosity shown in Figure 3d.

The roll-off corresponds to an approach toward a third dynamic regime, which occurs when the target strain wave is sufficiently slow, or the springs can sufficiently overcome the drag resistance to follow the target strain wave very closely, with little deviation from equilibrium. In this "quasi-static" limit, there is no dependence of $\dot{\lambda}_{\max}$ on either the stiffness or drag since the contraction speed is solely determined by the speed of the target strain wave. This regime occurs in the slow wave model when $\zeta \gg 1$, explaining the approach toward $\dot{\lambda}_{\max} = 1$ for large $\eta_{w,m}$ and small $\eta_{w,d}$ in Figures 3c and d. The three scaling regimes—the quench regime ($\dot{\lambda}_{\max} \sim \nu^{-1}$), the intermediate regime ($\dot{\lambda}_{\max} \sim \nu^{-1/2}$), and the quasi-static regime ($\dot{\lambda}_{\max} \sim \nu^{0}$)—fully characterize the qualitative dynamical behavior of myoneme contraction.

To summarize the dynamical behavior of the system as a function of $\eta_{w,d}$ and $\eta_{w,m}$, in *Appendix Supplementary methods* Section B 5 we introduce the dimensionless quantity χ, which measures the peak elastic energy stored in the system as a fraction of the maximum possible energy which is achieved in the quench limit. In Figure 3e we plot χ over $\eta_{w,m} \in [1/32, 32]$ and $\eta_{w,d} \in [1/4, 256]$, and In *Appendix* Figure 8 we show corresponding trajectories of the energy and length for these conditions.

Let us imagine fixing all parameters except the spring stiffness and the viscosity. Figure 3e then illustrates the system's ability to respond to the target strain wave under different mechanical and environmental conditions: for small $\eta_{w,m}$, corresponding to soft springs, the system stores a large fraction of the possible amount of internal energy ($\chi \approx 1$), but this fraction decreases as the drag, proportional to $\eta_{w,d}$, decreases. By contrast, for large $\eta_{w,m}$, the springs closely follow the target strain wave and never accumulate much internal energy ($\chi \approx 0$), and the amount that does accumulate decreases as the drag decreases. This energetic perspective thus provides a unified way to understand the dynamic regimes for organisms using Ca^{2+} motion.

IV. DISCUSSION

Summary. We present a minimal mathematical model of myoneme contraction that can capture kinematic features of the organisms *Spirostomum* and *Vorticella*, which have different shapes, sizes, and myoneme arrangements. Using an auxiliary reaction-diffusion model for the underlying Ca^{2+} dynamics, we provide scaling relationships for the width and speed of the target strain wave that enters the mechanical model. Through nondimensionalization, we identify the minimal independent set of parameters controlling contraction, and we further consider two limiting cases: a quench limit and a slow wave limit. The latter approximately applies to both *Spirostomum* and *Vorticella* in water, as determined by fits of the model to experimentally obtained length trajectories. The dynamics in this limit are formally mapped to the well-studied diffusion equation, with the role of diffusion constant played by the unitless parameter ζ. Analysis of the model shows that there are three dynamic regimes in which myoneme contraction can occur. The kinematic signatures of these regimes include the symmetry of contraction about the organism's midpoint and the exponent with which the maximum contraction velocity scales with viscosity. We additionally distinguish these regimes by a single quantity representing the peak elastic energy stored in the organism relative to the maximal possible value attained in the quench limit.

Biological implications of dynamic regimes. It is worthwhile to consider the possible biological implications of the three dynamic regimes. In the quasi-static regime, the myoneme contractile apparatus remains at mechanical equilibrium while the Ca^{2+} wave traverses the organism's length. In this limit, the contractile speed is fully determined by the wave speed V and does not scale with other parameters. The dissipation of chemical energy is minimized at the expense of the speed of motion. The marine protist *Acantharia* reportedly has myoneme-based spicules that are used to regulate buoyancy by contracting in a Ca^{2+}-powered process that is two orders of magnitude slower than contraction in *Spirostomum* or *Vorticella*[15,25]. In this case, contraction may occur quasi-statically. Conversely, the quench regime attains the highest contractile velocities. These high speeds consequently dissipate the most energy because the myoneme apparatus deviates the furthest from mechanical equilibrium. This regime would be suited to processes in which large speeds are physiologically important. For example, *Spirostomum* excites contraction of nearby organisms through "hydrodynamic trigger waves," requiring it to move sufficiently rapidly to disturb the fluid, dissipating energy in the process[10]. The intermediate regime, where we place the contraction of *Vorticella* and *Spirostomum*, is expected to achieve a balance between thermodynamic efficiency and biological functionality. While myoneme-based systems are predominantly found in ciliated protists, similar ATP-independent contractile protein networks exist in a wide range of other organisms across taxa, facilitating a diverse set of biological functions[8–23]. If similar mechanochemical dynamics apply in those organisms, then various selection pressures may favor a particular regime for each function.

Comparison to traditional latch-mediated systems. The theory of latch-mediated spring actuation (LaMSA) provides a general description of motion characterized by a fast unlatching event that releases stored elastic energy[60,61]. It has been applied to analyze macroscopic biomechanical processes like the striking of a Mantis shrimp's claw and a human finger snap[62,63]. One may expect that LaMSA explains myoneme-based contraction, with the "latch" release triggered by Ca^{2+} binding. However, LaMSA is designed to apply to macroscopic systems, neglecting the strong dissipative forces which are unavoidable at the cellular level. In addition, in myoneme contraction Ca^{2+} binding occurs over a spatially extended elastic domain, compared to the discrete mechanical elements considered in LaMSA. The qualitative features of traditional LaMSA systems compared to the myoneme-based "chemical latch" are illustrated in Figure 6. Outside the quench limit, the Ca^{2+} wave, which loads mechanical energy into the system, has a finite traversal time. This means that the system can begin relaxing before the energy has been fully loaded. This is a key distinction from traditional LaMSA systems, which are assumed to be fully loaded before relaxing. LaMSA systems also include a constraint force, which is lacking in free-swimming organisms like *Spirostomum*. Exploring the implications of adding constraint forces to myoneme-based systems would be an interesting direction for future research. For example, fixing the ends of *Spirostomum* and then releasing them after the Ca^{2+} wave has passed would allow artificially pushing the contraction process into the quench regime. Although how *physical* latches mediate energy flow has only recently been appreciated in biology[61], our model offers a guiding framework for how a *chemical* latch dynamically controls and tunes force output in ultrafast single-cell organisms.

Implications for synthetic biology. Finally, this model provides insights that may be useful to engineer myoneme-based synthetic systems. The feasibility of re-

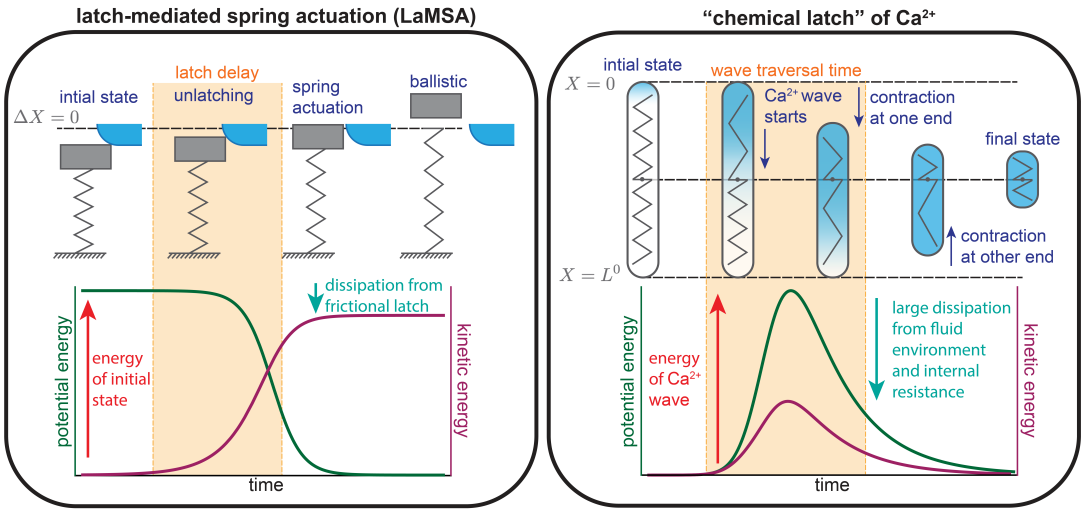

FIG. 6. **Schematic illustration of a chemical latch**. The left panel, adapted from Ref. 60, illustrates a mechanical latch-and-spring system. A latch, shown in blue, slides frictionally off of a compressed spring, shown in gray, which allows for a fast release of the stored potential energy. The finite time during which the latch slides is highlighted in orange. The potential and kinetic energies of the system are schematically plotted at the bottom. At smaller scales, such as the scale of a single-cell organism like *Spirostomum*, a different paradigm accounts for the chemical nature of mechanical activation (via a traveling Ca^{2+} wave). This is illustrated in the right panel, where analogous features of the dynamics in the macroscopic case are shown in the corresponding colors. The traveling wave is shown as a blue gradient, which controls the local rest length (indicated as the number of ridges) of internal springs, shown in gray.

constituting myoneme *in vitro* and exogenously controlling it using light-patterned Ca^{2+} release has recently been demonstrated[64]. Myoneme-based systems thus provide a mechanism for exogenously exerting mechanical forces at subcellular scales, with orthogonal chemistry to light-controllable actomyosin and kinesin-microtubule systems[65–69]. Our model reveals several vital parameters that can tune the dynamics of myoneme contraction. For instance, increasing cross-linking would increase the effective α, increasing the solution viscosity would increase the effective μ, and increasing the effective light-activated Ca^{2+} release rate or reducing Ca^{2+} buffering (thereby increasing D_C) would tune V and W of the target strain wave. Controlling these experimental parameters can allow exploring the different regimes identified in this work, thereby facilitating the design of synthetic cells with myoneme-based artificial cytoskeletons.

V. MATERIALS AND METHODS

A. Ca^{2+} dynamics

The dependence of the target strain $g(S,T)$ on the local bound Ca^{2+} concentration may be modeled using the instantaneous linear relation[45]

$$g(S,T) = 1 - (1 - g_{\min})\frac{B(S,T)}{B_{\text{tot}}}, \tag{17}$$

where $B(S,T)$ is the local concentration of Ca^{2+} bound to myoneme fibers and B_{tot} is the total concentration of binding sites (which is assumed to be uniform over the spatial domain). Finding $g(S,T)$ then requires specifying the dynamics for the bound Ca^{2+} profile $B(S,T)$. To avoid introducing extra variables, we first analyze the complete dynamics for $B(S,T)$ by extending a tractable model for a traveling Ca^{2+} wave developed by Kupferman *et al.* in Ref. 56, and we then use results of this analysis to determine an approximate form for $g(S,T)$ to use in the mechanical model.

The Kupferman model for a traveling Ca^{2+} wave is

$$\partial_T C = D_C \partial_S^2 C - \Gamma C + J\Theta(C - C_0). \tag{18}$$

Here, $C(S,T)$ is the concentration profile of cytosolic Ca^{2+} which diffuses with a diffusion constant D_C, leaks from the cytosolic compartment with a first-order rate constant Γ, and is released into the cytosol by internal stores at a spatially dependent rate $J\Theta(C - C_0)$. This last term involves a Heaviside function $\Theta(C - C_0)$, which approximates the kinetics of calcium-induced calcium release[70]. It "turns on" when the local Ca^{2+} concentration $C(S,T)$ exceeds a spatially uniform threshold C_0, at which point Ca^{2+} is released into the cytosol at a rate J. The authors of Ref. 56 show that the speed of the traveling wave is given by Eq. (5).

We extend the Kupferman model to allow cytosolic Ca^{2+} to bind to the myoneme assembly. This introduces the variable $B(S,T)$ for the local concentration of myoneme-bound Ca^{2+}, and the coupled dynamical equa-

tions for C and B are

$$\partial_T C = D_C \partial_S^2 C - \Gamma C + J\Theta(C - C_0) - K_+ C(B_{\rm tot} - B) + K_- B \quad (19)$$

$$\partial_T B = K_+ C(B_{\rm tot} - B) - K_- B. \quad (20)$$

Here, K_+ is the second-order rate constant for binding of cytosolic Ca^{2+} to open myoneme binding sites, which have concentration $B_{\rm tot} - B$. K_- is the first-order rate constant for the subsequent unbinding of myoneme-bound Ca^{2+}.

In *Appendix Supplementary methods* Section B 3, we analyze Eq. (B18) and Eq. (B19) under mild simplifying assumptions to show that: *i*) the function $B(S,T)$ is well approximated by a traveling wave with a sigmoidal profile:

$$\frac{B(S,T)}{B_{\rm tot}} = 1 - \frac{1}{1 + e^{-(S-VT)/W}}, \quad (21)$$

ii) its speed V is equal to the speed of diffusing Ca^{2+} wave (cf. Eq. (5)), and *iii*) its width W can be expressed in terms of the chemical parameters according to Eq. (B31).

Combing Eqs. (17) and (21) gives the following form for the non-autonomous target strain:

$$g(S,T) = g^*(S - VT) = g_{\rm min} + \frac{1 - g_{\rm min}}{1 + e^{-(S-VT+O)/W}}. \quad (22)$$

The additional parameter O is a length that allows an adjustable offset between $T = 0$ and the time $T = O$ when the center of the wave arrives at $S = 0$. This allows shifting time to achieve acceptable numerical agreement between boundary and initial conditions, as described in *Materials and methods* Section V B.

B. Computational methods

All numerical integration was performed with Mathematica's NDSolve function, using the method of lines option with a spatial discretization based on tensor product grids. The accuracy and precision goals were set high enough to ensure reasonable numerical convergence. To achieve agreement between the initial conditions Eq. (4) and the boundary conditions Eq. (3), we increased the parameter O in Eq. (22) (o in the non-dimensional model) so that $g(S,0) \approx 1$ across the computational domain. To solve the quench model Eq. (15), we evaluate the exact solution given in *Appendix* Eq. (B35) using 50 terms in the Fourier expansion.

C. Experimental methods

We obtained *Spirostomum* organisms from Carolina Biological and cultured them at room temperature. We prepared culturing medium by mixing one part boiled hay medium solution (Ward's Science, 470177-390), four parts boiled spring water, and two boiled wheat grains (Carolina, Item #132425) as described previously[32]. We inoculated organisms into fresh media approximately twice per week. For imaging, we pipetted several organisms at a time into microscopy slides with multiple channels (Ibidi, μ-Slide VI 0.4) or with multiple wells (Ibidi, μ-Slide 8 well). The channels are 400 μm high, allowing the organisms to swim and contract without confinement.

Our *Vorticella* samples were collected from Morse Pond near the Marine Biological Laboratory. We dissected small pieces of plant material to which individual or small groups of *Vorticella* were attached. We added these pieces of plant matter, along with enough imaging medium to cover them, into 8 well coverslip-bottomed sample chambers (Ibidi, μ-Slide 8 well).

To alter the viscosity, we prepared stock solutions of Ficoll PM 400 (Sigma F4375) in water and diluted them to concentrations between 3% and 12% (weight per volume). In the case of *Spirostomum*, we pipetted organisms directly into the Ficoll solution. In the case of *Vorticella*, we rinsed the samples several times with the solution within the sample chamber to ensure that the appropriate viscosity was reached. In both cases, slow pipetting was important to prevent shearing of the organisms in the high-viscosity solutions. To calculate viscosity ν as a function of percentage p of Ficoll in water we used the calibration function $\nu = e^{0.162p}$ reported in Refs. 71,72.

We performed brightfield imaging on either a Zeiss inverted microscope equipped with a 0.55 NA condenser, a 0.63x defocusing lens, DIC optics, and a 10x air objective or a Nikon Ti2 equipped with a 2x (MRD70020) or 10x (MRD70170) air objective. In both cases, we collected images using a pco.dimax CS camera equipped with at at least 2000 and up to 10,000 Hz.

For quantifying *Spirostomum* images, we first used Fiji[73] to threshold the organisms, and then we used Matlab to run Morphometrics[74] to obtain the cell contours. We used the pill-mesh option of Morphometrics to obtain cell shape and length.

For quantifying *Vorticella* length over time, we manually tracked the position of the end of the stalk attached to the cell body using home-built Python software.

ACKNOWLEDGMENTS

We wish to thank Shane Terrell for help setting up the experiments, Vincent Boudreau for providing samples of *Vorticella* in fresh pond water, Joe Brzostowski, Tanner Fadero, and Sam Lord for technical assistance with the microscopy, KC Huang and Tristan Ursell for providing the Morphometrics software, and Joe Lannan, Christian Pagán-Medina, Joël Lemière, and Jane Maienschein for helpful discussions. This work was mainly supported by National Science Foundation awards EF-1935260, EF-1935261, and EF-1935262. SV was supported by the National Institute Of General Medical Sci-

ences of the National Institutes of Health under Award Number R35GM147400. The content is solely the responsibility of the authors and does not necessarily represent the official views of the National Institutes of Health. CF acknowledges support from the University of Chicago through a Chicago Center for Theoretical Chemistry Fellowship. MSB acknowledges funding support from NIH Grant R35GM142588; NSF Grant 1817334; NSF CAREER 1941933; and a gift from the Open Philanthropy Project. FC acknowledges funding support from NIH Grant R35GM14179. We acknowledge the University of Chicago's Research Computing Center for computing resources, the Marine Biological Laboratory Whitman Summer Investigator Program and the Physiology Course for the use of microscopy equipment, and Zeiss and pco. for loans of cameras.

Appendix A: Supplementary results

1. Supplementary figures

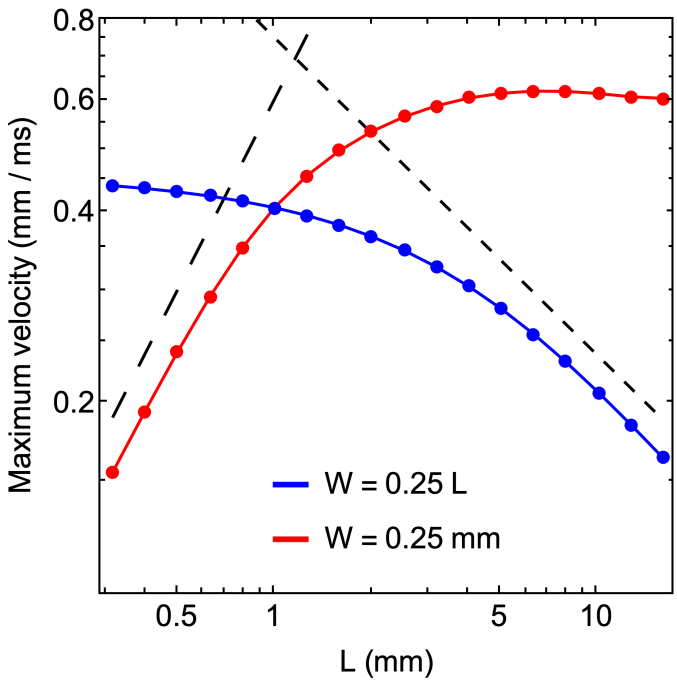

FIG. 7. **Coupling between length and width affects scaling.** In the dimensional model, Eq. (2) of the main text, the maximum contraction velocity $\dot{L}_{\max} = \max_T \dot{L}(T)$ is plotted as we vary the uncontracted length L. The red points correspond to conditions in which the width of the strain wave is fixed at $W = 0.25$ mm, while the blue points correspond to conditions in which the wave width scales with L as $W = 0.25\ L$. The varying of W with L qualitatively changes the dependence of $\max_T |\partial_T L|$ on L. The remaining parameters used for this plot are $\alpha = 1$ (mm/ms)^2, $\mu = 3$ ms^{-1}, $V = 0.5$ mm/ms, and $g_{\min} = 0$. The short and long dashed lines are proportional to $L^{-1/2}$ and L, respectively. See Ref. 37 for a corresponding experimental study on *Vorticella*.

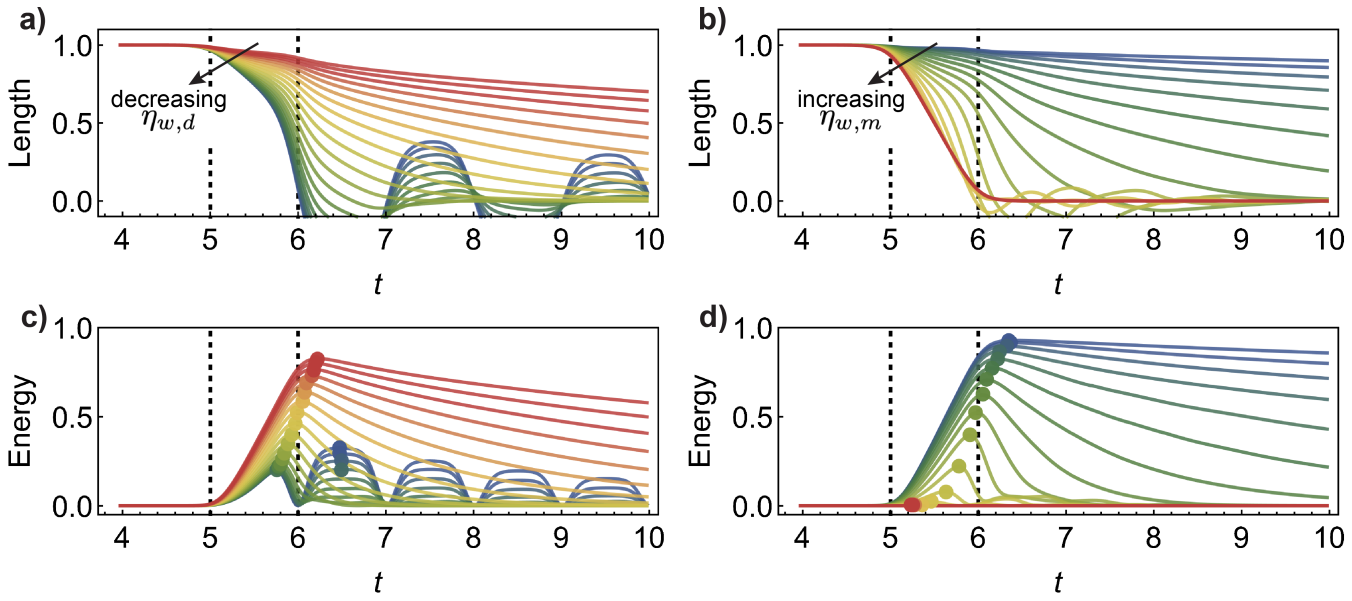

FIG. 8. **Dependence of length and energy trajectories on key timescales.** In panels (a) and (c), $\eta_{w,d}$ is varied from 0.25 to 256 in powers of $\sqrt{2}$ as the colors range from blue to red, with $\eta_{w,m} = 1$ fixed. The dimensionless length $\lambda(t)$ and energy $u(t)$ trajectories are shown; see the main text and *Appendix Supplementary methods* Section B 5 for a definition of u. The circles drawn in panel (c) show the values of $u_{\max}$ which are used to compute γ in Figure 3e of the main text (see SIAppendix Eq. (B44)). Similarly, in panels (b), and (d), $\eta_{w,m}$ is varied from 0.0625 to 32 in powers of $\sqrt{2}$ as the colors range from blue to red, with $\eta_{w,d} = 2$ fixed.

2. Fitted parameters

Here we fit the model (Eq. (2) in the main text) to each of the five length trajectories of *Spirostomum* shown in Figure 2a of the main text. Figure 9 illustrates these fits, and the fit parameters are given in Table I.

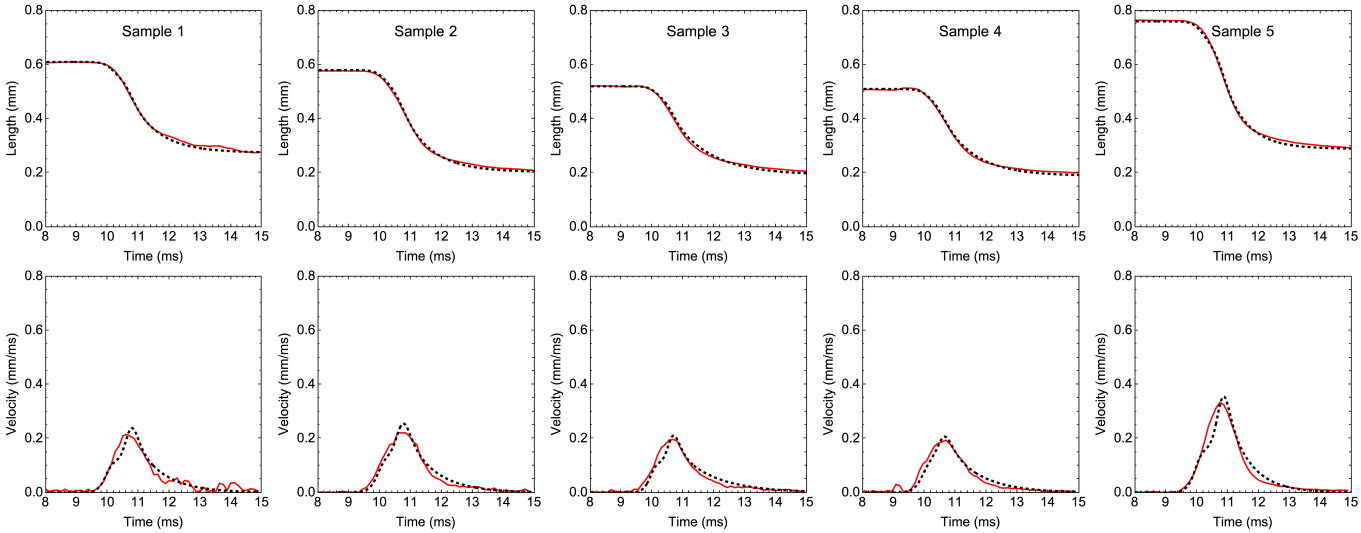

FIG. 9. **Fits for *Spirostomum*.** Experimental trajectories of length and velocity are shown as red curves, and fitted model solutions are shown as dashed black curves for the five samples in Figure 2a and b of the main text.

Parameter	Sample 1	Sample 2	Sample 3	Sample 4	Sample 5
L (mm)	0.61	0.58	0.52	0.51	0.76
μ/α (ms/mm^2)	25	28	45	40	14
$g_{\min}$	0.45	0.35	0.37	0.37	0.38
V (mm/ms)	0.8	0.8	0.8	0.85	0.9
W (mm)	0.11	0.12	0.1	0.13	0.13
$\eta_{w,d} = \mu L/V$	19.1	20.3	29.3	24.0	11.8
$\eta_{w,m} = \sqrt{\alpha}/V$	1.25	1.25	1.25	1.2	1.1
$\eta_{m,d} = \mu\sqrt{\alpha}/L$	13.6	16.7	27.4	28.3	6.6
$\zeta = \alpha/V\mu L$	0.082	0.077	0.054	0.058	0.11

TABLE I. **Estimated parameters for *Spirostomum*.** The fitted model parameters for the five contraction samples are shown in Figure 9. Four non-dimensional quantities are also computed for each sample.

We next fit the five length trajectories of *Vorticella* shown in Figure 2c of the main text. Figure 10 illustrates these fits, and the fit parameters are given in Table II.

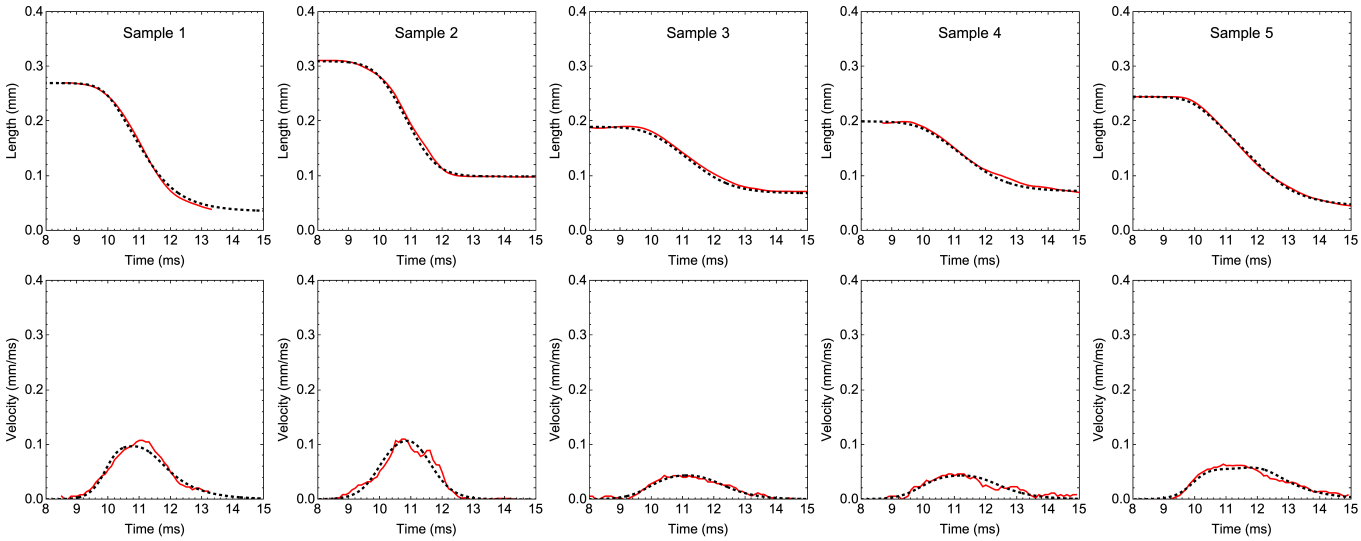

FIG. 10. **Fits for *Vorticella*.** Experimental trajectories of length and velocity are shown as red curves, and fitted model solutions are shown as dashed black curves for the five samples in Figure 2c and d of the main text.

Parameter	Sample 1	Sample 2	Sample 3	Sample 4	Sample 5
L (mm)	0.27	0.31	0.19	0.20	0.24
μ/α (ms/mm^2)	30	15	45	45	40
$g_{\min}$	0.13	0.32	0.36	0.36	0.18
V (mm/ms)	0.3	0.23	0.13	0.13	0.13
W (mm)	0.08	0.06	0.05	0.05	0.04
$\eta_{w,d} = \mu L/V$	27.0	12.4	65.8	69.2	75.4
$\eta_{w,m} = \sqrt{\alpha}/V$	3.3	4	7.7	7.7	7.7
$\eta_{m,d} = \mu\sqrt{\alpha}/L$	31.4	9.1	53.0	50.3	32.7
$\zeta = \alpha/V\mu L$	0.41	1.29	0.90	0.85	0.79

TABLE II. **Estimated parameters for *Vorticella*.** The fitted model parameters for the five contraction samples are shown in Figure 10. Four non-dimensional quantities are also computed for each sample.

To validate these estimates of the parameters, we compare to the mechanochemical parameters reported in Ref. 45 which were used in a detailed computational model of *Vorticella* that achieved good agreement with experiments. This comparison is summarized in Table III and shows reasonable agreement between our simplified description of the mechanics and a more detailed model.

In our fitting, we cannot determine α and μ independently given that, in the parameter regime in which we measured *Vorticella* and *Spirostomum* contraction, only the ratio μ/α is dynamically important. However, we can compare our estimated value for $\mu/\alpha = \widetilde{\gamma}/EA = \gamma/EAL$ to the corresponding quantity in Ref. 45, where E is Young's modulus, A is the cross-sectional area, and $\widetilde{\gamma}$ is the drag constant of the organism γ divided by its uncontracted length L. In their work, they estimate $E = 10^3$ Pa and $A = \pi\ 6.25 \times 10^{-6}$ mm^2 for the contractile stalk. To estimate the drag constant, we assume that drag is dominated by the contribution from the head (with diameter $D_{\rm h}$), which is subject to Stokes' law $\gamma = 3\pi D_{\rm h}\nu_{\rm w}$ where $\nu_{\rm w} = 10^{-3}$ Pa s is the viscosity of water. Using their estimate $L = 0.2$ mm, we obtain the value of μ/α reported in Table III.

Parameter	Present study	Ref. 45
L (mm)	0.25 ± 0.05	0.2
$g_{\min}$	0.27 ± 0.11	0.25
V (mm/ms)	0.19 ± 0.08	0.1
μ/α (ms/mm^2)	34 ± 14.7	120

TABLE III. **Estimated parameters for *Vorticella*.** The values reported for this study represent the mean and standard deviation of the five samples in Table II.

Appendix B: Supplementary methods

1. Derivation of continuum model

Here we derive the continuum model of myoneme contraction, Eq. (2) in the main text. We treat the system as a 1D chain of springs with open boundary conditions (or one end fixed for *Vorticella*) and non-autonomously determined rest lengths for each spring. We consider a set of N masses connected by $N-1$ springs, where the force on the ith mass is given by

$$m\partial_T^2 X_i = k\left(X_{i+1} - X_i - G_{i+\frac{1}{2}}\right) - k\left(X_i - X_{i-1} - G_{i-\frac{1}{2}}\right) - \gamma\partial_T X_i. \tag{B1}$$

Here, m is the mass, $X_i(T)$ is the horizontal position of mass i, T is time, k is the stiffness of every spring, $G_{i+\frac{1}{2}}(T)$ is the current rest length of the spring connecting masses i and $i+1$, and γ is the drag coefficient. We use capital letters for dimensional variables and lowercase letters for dimensionless variables. To pass to a continuum description, we label the material coordinate S and let the positions X_i and X_{i+1} be separated by a material distance δ which is assumed equal to the initial rest length $G_{i+\frac{1}{2}}(0)$ for each i. The original material length is L, so that $\delta = L/(N-1)$. We can rewrite Eq. (B1) as

$$\begin{aligned} m\partial_T^2 X(S,T) = k\Bigg(& X(S+\delta,T) - X(S,T) - G\left(S+\frac{\delta}{2},T\right) \\ & + X(S-\delta,T) - X(S,T) + G\left(S-\frac{\delta}{2},T\right)\Bigg) - \gamma\partial_T X(S,T). \end{aligned} \tag{B2}$$

We next assume δ is small and expand around $X(S,T)$ and $G(S,T)$. To second order in δ, this gives (suppressing the dependence on S and T for clarity)

$$\begin{aligned} m\partial_T^2 X &= k\Bigg(X + \delta\partial_S X + \frac{1}{2}\delta^2\partial_S^2 X - X - G - \frac{1}{2}\delta\partial_S G - \frac{1}{8}\delta^2\partial_S^2 G \\ &\quad + X - \delta\partial_S X + \frac{1}{2}\delta^2\partial_S^2 X - X + G - \frac{1}{2}\delta\partial_S G + \frac{1}{8}\delta^2\partial_S^2 G\Bigg) - \gamma\partial_T X \\ &= k\left(\delta^2\partial_S^2 X - \delta\partial_S G\right) - \gamma\partial_T X. \end{aligned} \tag{B3}$$

We switch to the dimensionless quantity $g(S,T) = G(S,T)/\delta$ representing the instantaneous rest length G divided by the material distance δ, which we call the local target strain. This gives

$$m\partial_T^2 X = k(\delta^2\partial_S^2 X - \delta^2\partial_S g) - \gamma\partial_T X. \tag{B4}$$

Next we introduce the constants $\widetilde{k} = k\delta$, $\widetilde{m} = m/\delta$, and $\widetilde{\gamma} = \gamma/\delta$, which represent how the stiffness, mass, and drag coefficient physically scale with the discretization length δ, and then take the limit $\delta \to 0$ such that all third and higher order terms in the expansion vanish. This gives

$$\partial_T^2 X - \alpha\left(\partial_S^2 X - \partial_S g\right) + \mu\partial_T X = 0 \tag{B5}$$

where $\alpha = \widetilde{k}/\widetilde{m}$ and $\mu = \widetilde{\gamma}/\widetilde{m} = \gamma/m$. The parameter α has units of velocity squared, and the parameter μ has units of inverse time.

We assume that at $T = 0$ the length of the organism linearly increases up to its undeformed material length, such that

$$X(S,0) = S. \tag{B6}$$

We also let it be at rest initially, such that

$$\partial_T X(S,0) = 0. \tag{B7}$$

We next consider the boundary conditions for Eq. (B5) at the edges of the domain, $S = 0,\ L$. In the case of *Spirostomum*, we take open boundary conditions at both ends, while for *Vorticella* we use the open condition at $S = 0$ and the Dirichlet condition $X(L,T) = L$. To derive the open boundary condition, we repeat the discretization steps

given above at the mass $i = 0$. We start with

$$m\partial_T^2 X_0 = k\left(X_1 - X_0 - G_{\frac{1}{2}}\right) - \gamma\partial_T X_0, \tag{B8}$$

and, passing to the continuous material coordinate S,

$$m\partial_T^2 X(0,T) = k\left(X(\delta,T) - X(0,T) - G\left(\frac{\delta}{2},T\right)\right) - \gamma\partial_T X(0,T). \tag{B9}$$

Upon expanding with respect to δ, we find (again dropping explicit argument dependence)

$$m\partial_T^2 X = k\left(\delta\partial_S X + \frac{1}{2}\delta^2\partial_S^2 X - G - \frac{1}{2}\delta\partial_S G - \frac{1}{8}\delta^2\partial_S^2 G\right) - \gamma\partial_T X. \tag{B10}$$

Introducing again α, μ, and g, we have

$$\partial_T^2 X = \alpha\left(\frac{1}{\delta}\partial_S X + \frac{1}{2}\partial_S^2 X - \frac{1}{\delta}g - \frac{1}{2}\partial_S g - \frac{1}{8}\delta^2\partial_S^2 g\right) - \mu\partial_T X. \tag{B11}$$

Taking the limit $\delta \to 0$ leaves us with the following condition at $S = 0$:

$$\partial_S X(0,T) = g(0,T). \tag{B12}$$

Note that the drag and inertial contributions to the force balance have not survived the limit in this case because the terms proportional to $\partial_S X$ and g do not cancel out in the expansion as they did in Eq. (B3), and these terms dominate as $\delta \to 0$. Through the same steps (or by symmetry considerations), we obtain an identical open condition applying at $S = L$.

2. Model justification and limitations

Our goal in this paper is to develop a general theory and intuition of myoneme contraction. Our model thus abstracts away numerous biological details which may be included in a more detailed computational model, such as the model in Ref. 45 for *Vorticella* contraction. Among several other presumably important physical features of the organisms, we have neglected possible volume or area conservation of the cells, any spatial variation in the drag coefficient along the cell's length[38,45], any twisting dynamics or three-dimensional geometry of the cell bodies[32,45], any braking dynamics contributed by the entanglement of the internal organelles[75], and any intermediate Reynolds number corrections to the viscous drag[38,45]. Our main justification for these omissions is that we are interested here in the one-dimensional compression dynamics of the myoneme mesh, neglecting for example the twist dynamics and anisotropic mesh contraction which have been observed in *Spirostomum*[32]. By neglecting the twist dynamics we do not allow for coupling between twisting and stretching, which is a feature of some biological materials like DNA. However, the magnitude of this coupling term tends to be much smaller than the stretching modulus (by a ratio of $\sim 1/10$ for DNA) and may be omitted in a minimal model[53]. Furthermore, our focus in this paper is on the contraction phase of *Spirostomum* and *Vorticella*, which is faster than the re-extension phase by two orders of magnitude. During this phase the forces are dominant along the contraction direction, which allows projecting out orthogonal dimensions. When considering the slower re-extension phase, however, one would need to consider additional details of the organism's three-dimensional geometry, as illustrated by the model in Ref. 45. Our simple treatment of the drag as Stokesian and uniform along the system's length could be straightforwardly refined by introducing a memory kernel for the force history or by letting the drag μ be a function of length $\mu(S)$. It was found experimentally that the Stokesian drag dominates the contribution from the memory term in *Vorticella*[38], however, and we find here that a uniform μ still allows semi-quantitative fits to experimental length trajectories. The dependence of the drag on the organisms' shapes (i.e. a cylindrical for *Spirostomum* and wine glass-shaped for *Vorticella*) could also be considered in future refinements of the model. Finally, we note that an interesting extension would be to introduce tension-gated Ca^{2+} channels in the chemical dynamics, to allow for two-way coupling between chemistry and mechanics[10]. This should allow for richer phenomenology to explore in the future.

3. Description of Ca^{2+} model

a. Review of Ca^{2+} models

There is a wide range of mathematical models that describe the time and space-dependent dynamics of intracellular Ca^{2+}, reviewed in Refs. 76 and 70. These dynamics are quite varied, including concentration patterns that are homogeneous in space but oscillatory in time, outward-propagating spirals, and the fast-traveling wavefronts which underlie mechanical contraction in *Spirostomum* and *Vorticella*[26,45–48]. An important process giving rise to these dynamics is calcium-induced calcium release (CICR), in which binding of Ca^{2+} to IP_3 and ryanodine receptor calcium channels causes them to release additional Ca^{2+}. This positive feedback does not continue indefinitely, as the probability of the channel being open (and hence its release rate) has a bell-shaped dependence on the logarithm of bound Ca^{2+}[76]. This dual role of Ca^{2+} inducing and subsequently inhibiting the channel release gives rise to the oscillatory patterns observed at long timescales. Given the speed of the traveling wave front in our case, however, it is sufficient to consider only the positive feedback.

Models of Ca^{2+} dynamics differ widely in their complexity, with the number of free parameters ranging from just a handful to more than a hundred[76]. Key features that distinguish Ca^{2+} models include:

- The number of separate species tracked (i.e., just cytosolic Ca^{2+} or also endoplasmic reticulum Ca^{2+} and intermediate signaling molecules like IP_3)
- Whether the channels are modeled as continuously or discretely distributed (with the latter choice found in the "fire-diffuse-fire" models[77,78])
- The level of detail for the CICR kinetics of Ca^{2+} channels, which are multimeric molecules that cooperatively bind Ca^{2+} and signaling molecules

With the goal in mind of constructing a minimal model of *Spirostomum* and *Vorticella*, and given the scarcity of experimentally measured kinetic parameters for these systems, we consider a highly simplified model which allows for traveling wave solutions and has clear interpretable parameters. Additionally, we opt for a continuous distribution of Ca^{2+} receptors (rather than a discrete fire-diffuse-fire description), as it is significantly more tractable. In the fire-diffuse-fire models, the continuous case is formally obtained as a limit of the discrete case when the release rate of Ca^{2+} is rate-limiting rather than the inter-receptor diffusion time[77,78].

b. Kuperfman model

For these reasons, we use the Kupferman model of Ref. 56 as the basis for our analysis of Ca^{2+} dynamics and its mechanical effects in *Spirostomum* and *Vorticella*. It tracks the cytosolic Ca^{2+} concentration as a function of time T and one space dimension S. Below, we also consider the concentration of myoneme-bound Ca^{2+}. In the laboratory frame, the reaction-diffusion dynamics for the cytosolic Ca^{2+} concentration C are

$$\partial_T C = D_C \partial_S^2 C - \Gamma C + J\Theta(C - C_0). \tag{B13}$$

Here, D_C is the Ca^{2+} diffusion constant in the cytosol, Γ is the first-order rate constant for Ca^{2+} leakage out of the cytosol, J is the rate of Ca^{2+} release by the open channels, and C_0 is the threshold concentration for the channel to open and begin releasing Ca^{2+}. Note that in this model of CICR, all of the complexity of cooperative binding of Ca^{2+} to the channels, dependence on local signaling molecule concentrations, and later inhibition of release is removed by assuming that the release rate dependence on Ca^{2+} concentration is captured by a Heaviside function $\Theta(C - C_0)$ (rather than some non-monotonic function which would be necessary to describe the dynamics on a longer timescale).

Eq. (B13) is rescaled in two steps: first, we non-dimensionalize and we then shift to the frame that is moving together with the traveling wave. The new non-dimensional variables c, t, and s are introduced by expressing concentration in units of $C_u \equiv C_0$, time in units of $T_u \equiv C_0/J$, and length in units of $S_u = \sqrt{C_0 D_C/J}$. The traveling frame is found by introducing the variable $u = s - vt$, where the traveling wave speed v is expressed in units of $V_u = \sqrt{JD_C/C_0}$. With this rescaling, Eq. (B13) becomes

$$\partial_u^2 c + v\partial_u c - \xi c + \Theta(c - 1) = 0, \tag{B14}$$

where $\xi \equiv C_0\Gamma/J$.

Eq. (B14) can be solved exactly, which is a key benefit of the Kupferman model[56]. The solution is

$$c(u) = \begin{cases} \frac{1}{\xi} + \frac{\xi-1}{\xi} e^{q^+ u} & u < 0 \\ e^{q^- u} & u > 0, \end{cases} \tag{B15}$$

where

$$q^{\pm} = \frac{1}{2}\left(-v \pm \sqrt{v^2 + 4\xi}\right) \tag{B16}$$

and

$$v = \frac{1 - 2\xi}{\sqrt{1-\xi}}. \tag{B17}$$

The point $u = 0$ is the boundary between the open ($u > 0$) and closed ($u < 0$) channels, such that at $u = 0$ we have $c = 1$. To obtain this solution to the ODE Eq. (B14) on the domains $(-\infty, 0)$ and $(0, \infty)$, the free constants were determined by the matching conditions $c(0^-) = c(0^+) = 1$ and $\partial_u c(0^-) = \partial_u c(0^+)$.

c. Width of myoneme-bound Ca^{2+} profile

We next extend the Kufperman model by introducing the concentration $B(S,T)$ of Ca^{2+} bound to myoneme proteins. Let B_{tot} be the conserved total concentration of myoneme binding sites, which is spatially uniform. When calcium totally saturates the available binding sites on myoneme, then $B = B_{\text{tot}}$. The new reaction-diffusion dynamics for C and B are

$$\partial_T C = D_C \partial_S^2 C - \Gamma C + J\Theta(C - C_0) - K_+ C(B_{\text{tot}} - B) + K_- B \tag{B18}$$

$$\partial_T B = K_+ C(B_{\text{tot}} - B) - K_- B. \tag{B19}$$

Here K_+ is the dimensional binding rate and K_- is the dimensional unbinding rate. We have assumed that the myoneme is immobile and hence the bound Ca^{2+} does not diffuse. The rescaled version of these equations is

$$\partial_u^2 c + v\partial_u c - \gamma c + \Theta(c-1) - k_+ c(b_{\text{tot}} - b) + k_+ b = 0 \tag{B20}$$

$$v\partial_u b + k_+ c(b_{\text{tot}} - b) - k_- b = 0, \tag{B21}$$

where $k_+ = K_+ C_0^2/J$, $k_- = K_- C_0/J$, $b = B/C_0$, and $b_{\text{tot}} = B_{\text{tot}}/C_0$.

By numerically integrating Eq. (B20) and Eq. (B21), we observed that the traveling profile of b has a width that depends on the binding kinetics determined by k_+ and k_- (see Figure 11 below). The width in turn affects the width of the strain profile $g(u)$, which can be modeled as a linear function of $b(u)$. The width of the strain profile $g(u)$ is an important feature governing the contraction dynamics in the mechanical model (see Figure 2e in the main text). Our goal here is to study how the width of the $b(u)$ profile depends on the kinetic parameters in Eq. (B20) and Eq. (B21).

Unfortunately, Eq. (B20) and Eq. (B21) are analytically intractable due to the non-linearity from the binding reaction. We, therefore, look for an approximate solution by relying on two assumptions:

1. The total myoneme concentration b_{tot} is sufficiently small that the dynamics of c do not depend on b.

2. In the range over which b is varying, around $u = 0$, the form of $c(u)$ is approximately linear.

Regarding the first assumption, we find numerically that increasing b_{tot} introduces small corrections to the predicted scaling behavior. Nonetheless, we can still gain insight into the model by assuming that the first assumption holds. Regarding the second assumption, we can check graphically that the profile of c is indeed roughly linear over the range where b is changing (although this also breaks down if b_{tot} is large). The linear approximation to $c(u)$ around $u = 0$ is

$$c(u) \approx 1 + \frac{\xi - 1}{\xi} q_+ u = 1 - u\sqrt{1-\xi}. \tag{B22}$$

This holds for both sides of the piecewise definition in Eq. (B15) since the derivatives are matched at $u = 0$. In this

approximation, $c(u)$ goes to zero at $u_0 = 1/\sqrt{1-\xi}$, and since b cannot be greater than zero if $c = 0$, then b must go to zero at that point as well.

With these assumptions we have

$$v\partial_u b + k_+(1 - u\sqrt{1-\xi})(b_{\text{tot}} - b) - k_- b = 0 \tag{B23}$$

which admits an exact solution:

$$\frac{b(u)}{b_{\text{tot}}} = 1 + A\exp\left(\frac{2(k_- + k_+)u - gk_+u^2}{2v}\right) + \frac{\sqrt{2}k_-}{h}\text{daw}\left(\frac{k_- + k_+ - gk_+s}{\sqrt{2}h}\right). \tag{B24}$$

Here, $g = \sqrt{1-\xi}$, $h = \sqrt{gk_+v}$, and daw is the Dawson function, defined as

$$\text{daw}\,(x) = e^{-x^2}\int_0^x e^{t^2}dt. \tag{B25}$$

The constant A can be fixed by requiring $b(u_0) = 0$, resulting in

$$\frac{b(u)}{b_{\text{tot}}} = 1 + \left(\frac{\sqrt{2}k_-}{h}\text{daw}\left(\frac{k_-}{\sqrt{2}h}\right) - 1\right)\exp\left(\frac{2(k_- + k_+)u - gk_+u^2}{2v}\right) - \frac{\sqrt{2}k_-}{h}\text{daw}\left(\frac{k_- + k_+ - gk_+u}{\sqrt{2}h}\right). \tag{B26}$$

This is defined for $u < u_0$, while for $u \geq u_0$, $b(u) = 0$. Eq. (B26) can be simplified because $k_-/h \ll 1$ for typical values of the parameters, while the Dawson function does not exceed 1 in absolute value. We can thus write

$$\frac{b(u)}{b_{\text{tot}}} \approx 1 - \exp\left(\frac{2(k_- + k_+)u - gk_+u^2}{2v}\right). \tag{B27}$$

Furthermore, the quadratic part of the exponent dominates after rescaling back to dimensional units, allowing us to finally write

$$\frac{b(u)}{b_{\text{tot}}} \approx 1 - \exp\left(-\frac{gk_+u^2}{2v}\right). \tag{B28}$$

This is a Gaussian function of u with a width given by $w = \sqrt{v/gk_+}$. In dimensional units, we have

$$\frac{k_+u^2}{v} = W^{-2}(S - VT)^2 \tag{B29}$$

where

$$W^{-2} = \frac{K_+}{V}\sqrt{\frac{C_0 J}{D_C}}. \tag{B30}$$

We can simplify using the fact that $V \approx \sqrt{JD_C/C_0}$ since ξ is typically small in Eq. (B17) and, by assumption, the dynamics of c do not depend on b. This gives the final result

$$W \approx \sqrt{\frac{D_C}{C_0K_+}}. \tag{B31}$$

Eq. (B31) predicts that the width W only depends on the three quantities D_C, C_0, and K_+. We confirm this numerically in the next section.

d. Numerical results

We demonstrate through numerical tests the accuracy of the above scaling form for W, Eq. (B31). Throughout this section and in the inset of Figure 2e in the main text, we use the following parameters unless noted otherwise.

Symbol	Value	Units
D_C	200	μm^2/s
C_0	0.5	μM
Γ	100	1/s
J	10^7	μM/s
K_+	0.5	1/μM s
K_-	0.15	1/s
B_{tot}	1000	μM

These parameters are mostly in keeping with those used in Ref. 56 except for K_+ and K_-, which are based on values roughly inferred for *Vorticella* from Ref. 45.

Using the numerical methods described in *Materials and methods* section V B of the main text, we numerically integrate the full chemical dynamics, Eq. (B18) and Eq. (B19), on a domain of length $L = 1000$ μm for 0.05 s, and we use the boundary condition $\partial_S C(0,T) = \partial_S C(L,T) = 0$. We initiate the wave by setting $C(S,0) = J/\Gamma$ on the segment $S \in [0, 100]$ and $B(S,0) = 0$ everywhere. To obtain W and test predicted scaling form in Eq. (B31), we fit to the profile $B(S, 0.005\text{ s})$ the sigmoidal function

$$B_{\text{fit}}(S) = 1 - \frac{1}{1 + e^{-\frac{S-O}{W}}} \tag{B32}$$

for the offset O and width W. Note that this functional form does not match the derived form in Eq. (B28) but nonetheless has a well-defined characteristic width. We favor using the sigmoidal approximation to the bound concentration profile because it does not involve a piecewise definition as the form in Eq. (B28) does (where $b(u) = 0$ for $u > 0$), making it much easier to work with. If the derived scaling is observed for the width of this function, it suggests that the width's scaling behavior does not depend on the specific functional form in Eq. (B28).

In Figure 11a we show the concentration profiles for C and B from $T = 0$ s to $T = 0.025$ s, illustrating the propagation of the diffusing and bound Ca^{2+} profiles. In Figure 11b we show these profiles at $T = 0.01$ s, along with the fit of Eq. (B32) to $B(S)$. Note that the profile for C is indeed approximately linear over the range where B is changing, validating our previous assumption. We show similar profiles for the condition when $K_+ = 0.125$ $(\mu\text{M } s)^{-1}$ and $D_C = 800$ μm^2/s (Figure 11c), and when $B_{\text{tot}} = 16,000$ μM (Figure 11d). In Figure 12 we show the scaling of W with the quantities K_+, K_-, D, C_0, Γ, and J. We predict from Eq. (B31) that the scaling exponents for these will be, respectively, $-1/2,\ 0,\ 1/2, -1/2,\ 0$, and 0, and these predictions are numerically confirmed.

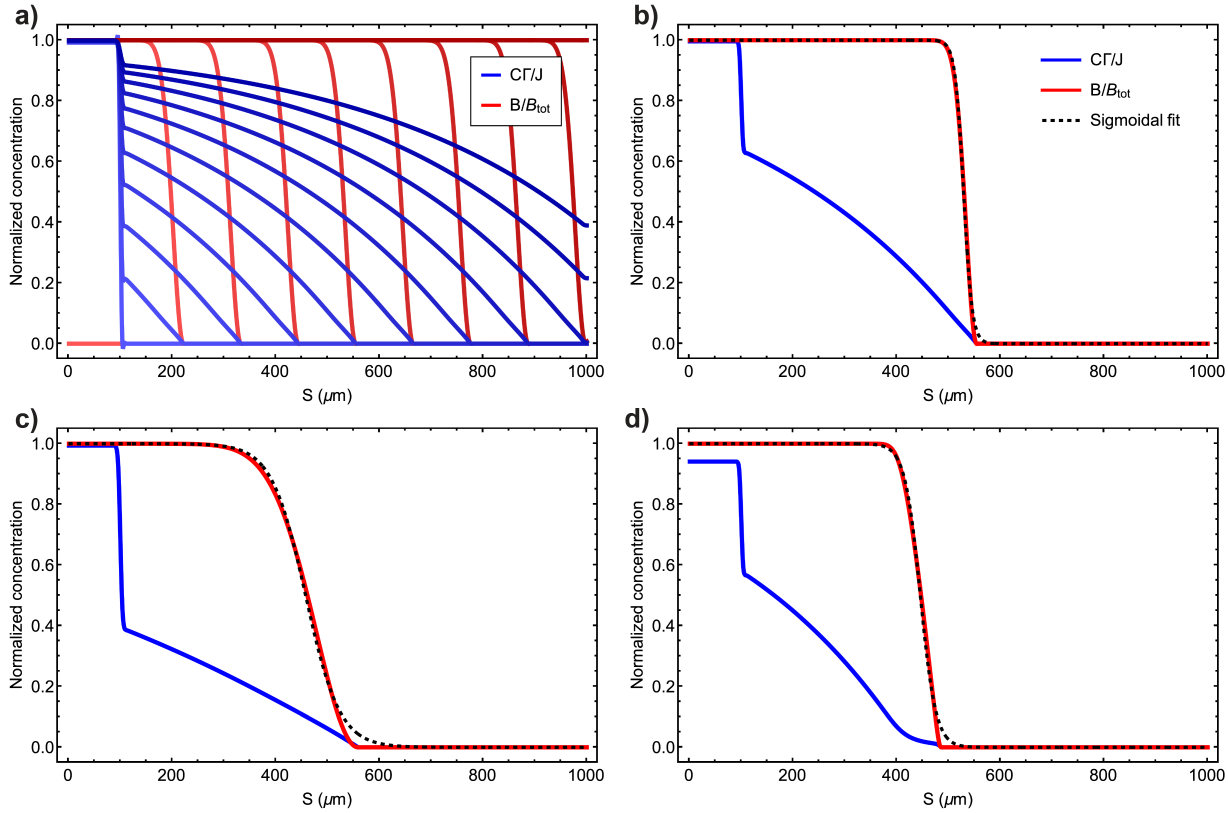

FIG. 11. **Numerical integration of** Eq. (B18) **and** Eq. (B19)**.** (a) The profiles of C and B from $T = 0$ s to $T = 0.025$ s in steps of 0.005 s as brightness ranges from light to dark. (b) The profiles of C and B at $T = 0.01$ s. The fit of Eq. (B32) to the profile of B is shown as a dashed black line. The fitted width of B is 8.2 μm. (c) The profiles of C and B at $T = 0.001$ s for the same parameters as in (a) but with $K_+ = 0.125$ (μM/s) and $D_C = 800$ (μm^2/s). The fitted width of B is 33.6 μm. (d) The profiles of C and B at $T = 0.01$ s for the same parameters as in (a) but with $B_{\rm tot} = 16,000$ μM. The fitted width of B is 15.0 μm.

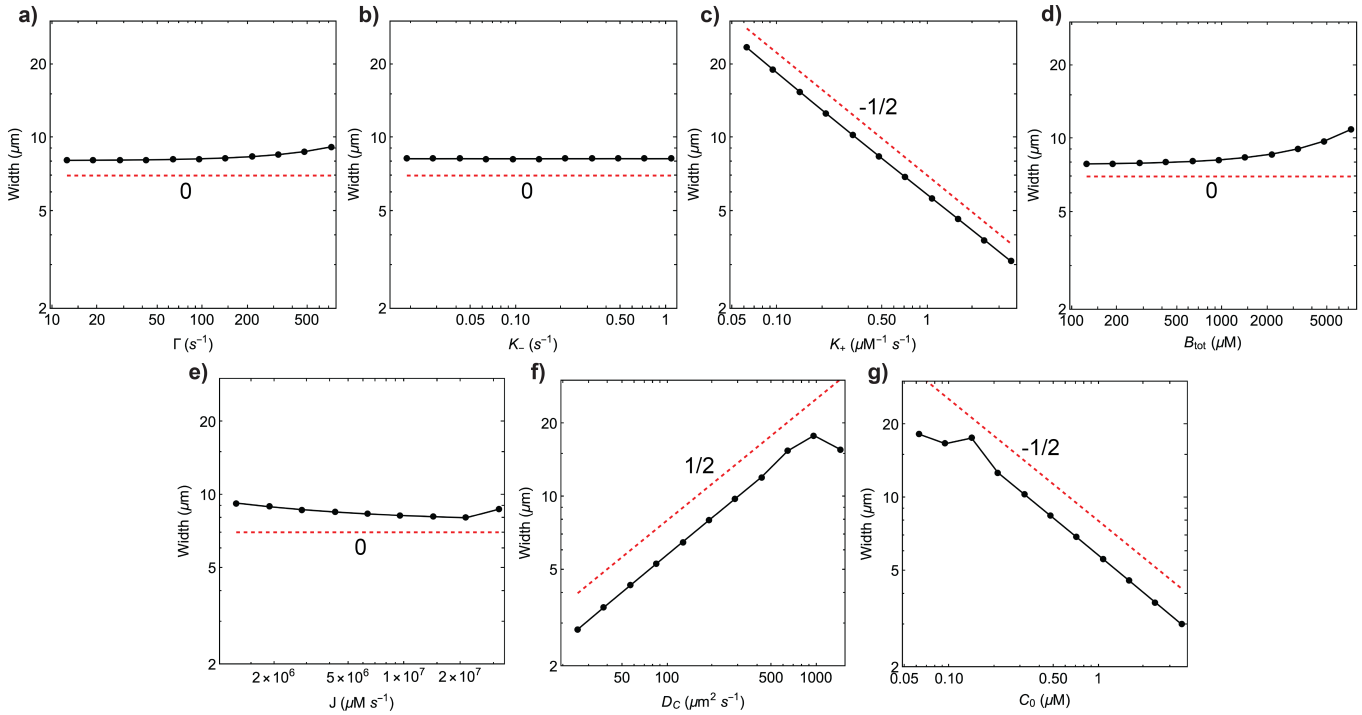

FIG. 12. **The scaling of W.** Results from fitting Eq. (B32) to $B(S, 0.005\text{ s})$, obtained from numerical integration, shown as connected black dots. The red dotted lines illustrate the predicted scaling from the analytical result $W \approx \sqrt{D_C/C_0 K_+}$.

4. Exact solution in the quench limit

The solution to Eq. (15) in the main text can be found exactly using a Fourier expansion. The initial condition is expanded as

$$y(s,0) = a_0 + \sum_{n=1}^{\infty} a_n \cos(n\pi s), \tag{B33}$$

where a_0 may be set to zero and

$$a_n = \int_0^1 y(s,0)\cos(n\pi s)ds. \tag{B34}$$

By linearity, the solution can then be written as

$$y(s,t) = \sum_{n=1}^{\infty} a_n y_n(s,t). \tag{B35}$$

The functions $y_n(s,t)$ can be found by solving Eq. (15) in the main text with the simplified initial conditions $y(s,0) = \cos(n\pi s)$, and the result is

$$y_n(s,t) = \cos(n\pi s) e^{-\frac{\eta_{m,d} t}{2}} \left(\cosh(t\beta_n/2) + \frac{\eta_{m,d} \sinh(t\beta_n/2)}{\beta_n} \right) \tag{B36}$$

where

$$\beta_n = \sqrt{\eta_{m,d}^2 - 4n^2\pi^2}. \tag{B37}$$

There is a similarity between the continuum quench model, whose dynamics are given in Eq. (15) of the main text,

and perhaps the simplest dissipative contraction dynamics which one could consider: the motion of a single mass attached by a spring to a wall, following sudden release from an initial fixed state. The position of the mass $z(t)$ obeys

$$\partial_t^2 z + \omega^2 z + \mu \partial_t z = 0 \tag{B38}$$

where $\omega = \sqrt{k/m}$ and $\mu = \gamma/m$ are defined in terms of the spring's stiffness k, mass m, and the drag coefficient γ. By rewriting $y_n(s,t)$ from Eq. (B36) as

$$y_n(s,t) = \cos(n\pi s) z_n(t) \tag{B39}$$

and using the solution of $y(s,t)$ from Eq. (B35), one can show that Eq. (15) in the main text is equivalent to

$$\sum_{n=1}^{\infty} a_n \cos(n\pi s) \left(\partial_t^2 z_n(t) + (n\pi)^2 z_n(t) + \eta_{m,d} \partial_t z_n(t)\right) = 0, \tag{B40}$$

which further implies that

$$\partial_t^2 z_n(t) + (n\pi)^2 z_n(t) + \eta_{m,d} \partial_t z_n(t) = 0 \tag{B41}$$

for each n. Thus, in the continuum quench model, each spatial harmonic of the initial deviation from equilibrium behaves like a damped spring with frequency $n\pi$ and drag $\eta_{m,d}$.

5. Energetics of contraction

Here we consider the energetics of myoneme contraction. The internal energy of the system is the sum of the energy of each spring in the chain. In the continuum limit this is (cf. Eq. (2))

$$U = \frac{EA}{2} \int_0^L (\partial_S X - g)^2 dS, \tag{B42}$$

using dimensional variables. The non-dimensional version is

$$u \equiv \frac{2U}{EAL} = \int_0^1 (\partial_s x - f)^2 ds = \int_0^1 h^2 ds, \tag{B43}$$

where we have absorbed the factor 1/2 into the definition of u for simplicity and used the definition of h in Eq. (12) of the main text. Trajectories of $l(t)$ and $u(t)$ are shown in SIAppendix Figure 8 for several values of the non-dimensional model parameters $\eta_{w,m}$ and $\eta_{w,d}$.

In the quench limit, the system starts at rest with $x = s$ and $f = 1$ and all springs then instantly take new rest lengths $g_{\min}$, causing the internal energy to jump discontinuously from $u = 0$ to $(1-g_{\min})^2$. We can regard $(1-g_{\min})^2$ as the maximum internal energy that the system can store in response to a target strain wave $g(s,t)$ taking values in $[g_{\min}, 1]$. Outside the quench limit, the system relaxes while the wave is traversing its length, and the maximum internal energy stored in the organism during the contraction trajectory $u_{\max} \equiv \max_t u(t)$ is less than $(1-g_{\min})^2$. We can therefore quantify how quench-like the dynamics are using

$$\chi \equiv \frac{u_{\max}}{(1-g_{\min})^2} \in (0,1). \tag{B44}$$

[1]Michael Murrell, Patrick W Oakes, Martin Lenz, and Margaret L Gardel. Forcing cells into shape: the mechanics of actomyosin contractility. *Nature Reviews Molecular Cell Biology*, 16(8):486–498, 2015.
[2]Wallace F Marshall. Don't blink: Observing the ultra-fast contraction of spasmonemes. *Biophysical Journal*, 94(1):4–5, 2008.
[3]T Weis-Fogh and WB Amos. Evidence for a new mechanism of cell motility. *Nature*, 236(5345):301–304, 1972.
[4]Jean Cachon and Monique Cachon. Movement by non-actin filament mechanisms. *Biosystems*, 14(3-4):313–326, 1981.
[5]Denis H Lynn. *The Ciliated Protozoa: Characterization, Classification, and Guide to the Literature*. Springer, 2008.
[6]WB Amos. Reversible mechanochemical cycle in the contraction of Vorticella. *Nature*, 229(5280):127–128, 1971.
[7]Sangjin Ryu, Rachel E Pepper, Moeto Nagai, and Danielle C France. Vorticella: a protozoan for bio-inspired engineering. *Micromachines*, 8(1):4, 2016.
[8]RB Hawkes and DV Holberton. Myonemal contraction of Spirostomum I. Kinetics of contraction and relaxation. *Journal of Cellular Physiology*, 84(2):225–235, 1974.
[9]RB Hawkes and DV Holberton. Myonemal contraction of spirostomum. II. Some mechanical properties of the contractile apparatus. *Journal of Cellular Physiology*, 85(3):595–602, 1975.
[10]Arnold JTM Mathijssen, Joshua Culver, M Saad Bhamla, and Manu Prakash. Collective intercellular communication through ultra-fast hydrodynamic trigger waves. *Nature*, 571(7766):560–564, 2019.
[11]Yasushige Moriyama, Hiroyuki Okamoto, and Hiroshi Asai. Rubber-like elasticity and volume changes in the isolated spasmoneme of giant Zoothamnium sp. under Ca^{2+}-induced contraction. *Biophysical Journal*, 76(2):993–1000, 1999.
[12]RB Moreton and WB Amos. Electrical recording from the contractile ciliate Zoothamnium geniculatum ayrton. *J. Exp. Biol.*, 83(1):159–167, 1979.
[13]Michael Melkonian, Peter L Beech, Christos Katsaros, and Dorothee Schulze. Centrin-mediated cell motility in algae. In *Algal Cell Motility*, pages 179–221. Springer, 1992.
[14]Masaki Ishida, Yoshinobu Shigenaka, and Koji Taneda. Studies on the mechanism of cell elongation in blepharisma japonicum I. A physiological mechanism how light stimulation evokes cell elongation. *European Journal of Protistology*, 25(2):182–186, 1989.
[15]Jean Febvre. The myoneme of the Acantharia (Protozoa): A new model of cellular motility. *Biosystems*, 14(3-4):327–336, 1981.
[16]Motonori Ando and Yoshinobu Shigenaka. Structure and function of the cytoskeleton in heliozoa: I. Mechanism of rapid axopodial contraction in echinosphaerium. *Cell Motil. Cytoskelet.*, 14(2):288–301, 1989.
[17]Bernard Viguès and Raghida Damaj. The adhesive disc in the mobilid ciliate trichodina pediculus: Evidence for centrin-related, calcium-sensitive filaments. *Cytoskeleton*, 69(2):113–124, 2012.
[18]M Kawachi and I Inouye. Ca^{2+}-mediated induction of the coiling of the haptonema in Chrysochromulina hirta (Prymnesiophyta= Haptophyta). *Phycologia*, 33(1):53–57, 1994.
[19]GI McFadden, D Schulze, B Surek, Jeffrey L Salisbury, and M Melkonian. Basal body reorientation mediated by a Ca^{2+}-modulated contractile protein. *Journal of Cell Biology*, 105(2):903–912, 1987.
[20]Jean Cachon and Monique Cachon. An unusual mechanism of cell contraction: Leptodiscinae dinoflagellates. *Cell Motility*, 4(1):41–55, 1984.
[21]Michael Knoblauch, Gundula A Noll, Torsten Müller, Dirk Prüfer, Ingrid Schneider-Hüther, Dörte Scharner, Aart JE Van Bel, and Winfried S Peters. ATP-independent contractile proteins from plants. *Nature Materials*, 2(9):600–603, 2003.
[22]Michael Knoblauch and Winfried S Peters. Forisomes, a novel type of Ca^{2+}-dependent contractile protein motor. *Cell Motil. Cytoskelet.*, 58(3):137–142, 2004.
[23]Wilhelm TS Huck. Responsive polymers for nanoscale actuation. *Materials Today*, 11(7-8):24–32, 2008.
[24]Hartmut Hoffmann-Berling. The mechanism of a new contraction cycle distinct from muscle contraction. *Biochimica et Biophysica Acta*, 27:247–255, 1958.
[25]Jean Febvre and Collete Febvre-Chevalier. Motility processes in acantharia (protozoa) iii. calcium regulation of the contraction-relaxation cycles of in vivo myonemes. *Biology of the Cell*, 67(3):251–261, 1989.
[26]KAORU Katoh and YUTAKA Naitoh. Control of cellular contraction by calcium in Vorticella. *J. Exp. Biol.*, 189(1):163–177, 1994.
[27]Yukiko Yokoyama and Hiroshi Asai. Contractility of the spasmoneme in glycerinated vorticella stalk induced by various divalent metal and lanthanide ions. *Cell Motil. Cytoskelet.*, 7(1):39–45, 1987.
[28]WB Amos. Structure and coiling of the stalk in the peritrich ciliates vorticella and carchesium. *Journal of Cell Science*, 10(1):95–122, 1972.
[29]L_M Routledge, WB Amos, BL Gupta, TA Hall, and T Weis-Fogh. Microprobe measurements of calcium binding in the contractile spasmoneme of a vorticellid. *Journal of Cell Science*, 19(1):195–201, 1975.
[30]Alick R Jones, Theodore L Jahn, and James R Fonseca. Contraction of protoplasm. I. Cinematographic analysis of the anodally stimulated contraction of Spirostomum ambiguum. *Journal of Cellular Physiology*, 68(2):127–133, 1966.
[31]Tsutomu Ochiai, Hiroshi Asai, and Keiji Fukui. Hysteresis of contraction-extension cycle of glycerinated Vorticella. *Journal of Protozoology*, 26(3):420–425, 1979.
[32]LX Xu and MS Bhamla. Biophysical mechanism of ultrafast helical twisting contraction in the giant unicellular ciliate Spirostomum ambiguum. *bioRxiv*, page 854836, 2019.
[33]Yasushige Moriyama, Shigeo Hiyama, and Hiroshi Asai. High-speed video cinematographic demonstration of stalk and zooid contraction of Vorticella convallaria. *Biophysical Journal*, 74(1):487–491, 1998.
[34]Sangjin Ryu and Paul Matsudaira. Unsteady motion, finite Reynolds numbers, and wall effect on Vorticella convallaria contribute contraction force greater than the stokes drag. *Biophysical Journal*, 98(11):2574–2581, 2010.
[35]Sangjin Ryu, Matthew J Lang, and Paul Matsudaira. Maximal force characteristics of the Ca^{2+}-powered actuator of Vorticella convallaria. *Biophysical Journal*, 103(5):860–867, 2012.
[36]Jiazhong Zhou, Sangjin Ryu, and David Admiraal. Flow and transport effect caused by the stalk contraction cycle of Vorticella convallaria. *Biomicrofluidics*, 11(3):034119, 2017.
[37]Eun Gul Chung and Sangjin Ryu. Stalk-length-dependence of the contractility of Vorticella convallaria. *Physical Biology*, 14(6):066002, 2017.
[38]A Upadhyaya, M Baraban, J Wong, P Matsudaira, A Van Oudenaarden, and L Mahadevan. Power-limited contraction dynamics of Vorticella convallaria: an ultrafast biological spring. *Biophysical Journal*, 94(1):265–272, 2008.
[39]M Cristina Marchetti, Jean-François Joanny, Sriram Ramaswamy, Tanniemola B Liverpool, Jacques Prost, Madan Rao, and R Aditi Simha. Hydrodynamics of soft active matter. *Reviews of Modern Physics*, 85(3):1143, 2013.

[40]Gaudenz Danuser, Jun Allard, and Alex Mogilner. Mathematical modeling of eukaryotic cell migration: insights beyond experiments. *Annual review of cell and developmental biology*, 29:501, 2013.
[41]Jacques Prost, Frank Jülicher, and Jean-François Joanny. Active gel physics. *Nature physics*, 11(2):111–117, 2015.
[42]Konstantin Popov, James Komianos, and Garegin A Papoian. Medyan: Mechanochemical simulations of contraction and polarity alignment in actomyosin networks. *PLoS computational biology*, 12(4):e1004877, 2016.
[43]Simon L Freedman, Shiladitya Banerjee, Glen M Hocky, and Aaron R Dinner. A versatile framework for simulating the dynamic mechanical structure of cytoskeletal networks. *Biophysical Journal*, 113(2):448–460, 2017.
[44]FJ Nédélec, Thomas Surrey, Anthony C Maggs, and Stanislas Leibler. Self-organization of microtubules and motors. *Nature*, 389(6648):305–308, 1997.
[45]Gaurav Misra, Richard B Dickinson, and Anthony JC Ladd. Mechanics of Vorticella contraction. *Biophysical Journal*, 98(12):2923–2932, 2010.
[46]KAORU Katoh and MUNEHIRO Kikuyama. An all-or-nothing rise in cytosolic. *J. Exp. Biol.*, 200(1):35–40, 1997.
[47]HISASHI Shiono and YUTAKA Naitoh. Cellular contraction precedes membrane depolarization in Vorticella convallaria. *J. Exp. Biol.*, 200(16):2249–2261, 1997.
[48]Igor Delvendahl, Lukasz Jablonski, Carolin Baade, Victor Matveev, Erwin Neher, and Stefan Hallermann. Reduced endogenous Ca^{2+} buffering speeds active zone Ca^{2+} signaling. *Proceedings of the National Academy of Sciences*, 112(23):E3075–E3084, 2015.
[49]L Mahadevan and P Matsudaira. Motility powered by supramolecular springs and ratchets. *Science*, 288(5463):95–99, 2000.
[50]Ferenc Horkay. Polyelectrolyte gels: a unique class of soft materials. *Gels*, 7(3):102, 2021.
[51]Alex Mogilner and George Oster. Polymer motors: pushing out the front and pulling up the back. *Current Biology*, 13(18):R721–R733, 2003.
[52]William S Slaughter. *The Linearized Theory of Elasticity*. Springer Science & Business Media, 2012.
[53]Jeff Gore, Zev Bryant, Marcelo Nöllmann, Mai U Le, Nicholas R Cozzarelli, and Carlos Bustamante. DNA overwinds when stretched. *Nature*, 442(7104):836–839, 2006.
[54]Carlos Floyd, Haoran Ni, Ravinda S Gunaratne, Radek Erban, and Garegin A Papoian. On stretching, bending, shearing, and twisting of actin filaments i: Variational models. *Journal of Chemical Theory and Computation*, 18(8):4865–4878, 2022.
[55]Lawrence E Kinsler, Austin R Frey, Alan B Coppens, and James V Sanders. *Fundamentals of Acoustics*. John wiley & sons, 2000.
[56]Raz Kupferman, Partha P Mitra, PC Hohenberg, and SS Wang. Analytical calculation of intracellular calcium wave characteristics. *Biophysical Journal*, 72(6):2430–2444, 1997.
[57]Hideki Ishida, Toshinobu Suzaki, and Yoshinobu Shigenaka. Effect of mg2+ on ca2+-dependent contraction of a spirostomum cell model. *European Journal of Protistology*, 32(3):316–319, 1996.
[58]Earl M Ettienne. Control of contractility in Spirostomum by dissociated calcium ions. *Journal of General Physiology*, 56(2):168–179, 1970.
[59]Ankit Rohatgi. Webplotdigitizer, 2017.
[60]Sathvik Divi, Xiaotian Ma, Mark Ilton, Ryan St. Pierre, Babak Eslami, SN Patek, and Sarah Bergbreiter. Latch-based control of energy output in spring actuated systems. *Journal of the Royal Society Interface*, 17(168):20200070, 2020.
[61]Mark Ilton, M Saad Bhamla, Xiaotian Ma, Suzanne M Cox, Leah L Fitchett, Yongjin Kim, Je-sung Koh, Deepak Krishnamurthy, Chi-Yun Kuo, Fatma Zeynep Temel, et al. The principles of cascading power limits in small, fast biological and engineered systems. *Science*, 360(6387):eaao1082, 2018.
[62]Emma Steinhardt, Nak-seung P Hyun, Je-sung Koh, Gregory Freeburn, Michelle H Rosen, Fatma Zeynep Temel, SN Patek, and Robert J Wood. A physical model of mantis shrimp for exploring the dynamics of ultrafast systems. *Proceedings of the National Academy of Sciences*, 118(33):e2026833118, 2021.
[63]Raghav Acharya, Elio J Challita, Mark Ilton, and M Saad Bhamla. The ultrafast snap of a finger is mediated by skin friction. *Journal of the Royal Society Interface*, 18(184):20210672, 2021.
[64]Xiangting Lei, Tuhin Chakrabortty, Jerry Honts, and Saad Bhamla. In vitro light-controlled patterns and force generation for synthetic cytoskeletal networks. *Bulletin of the American Physical Society*, 2022.
[65]Muneaki Nakamura, Lu Chen, Stuart C Howes, Tony D Schindler, Eva Nogales, and Zev Bryant. Remote control of myosin and kinesin motors using light-activated gearshifting. *Nature Nanotechnology*, 9(9):693–697, 2014.
[66]Paul V Ruijgrok, Rajarshi P Ghosh, Sasha Zemsky, Muneaki Nakamura, Rui Gong, Lin Ning, Robert Chen, Vipul T Vachharajani, Alexander E Chu, Namrata Anand, et al. Optical control of fast and processive engineered myosins in vitro and in living cells. *Nature Chemical Biology*, 17(5):540–548, 2021.
[67]Rui Zhang, Steven A Redford, Paul V Ruijgrok, Nitin Kumar, Ali Mozaffari, Sasha Zemsky, Aaron R Dinner, Vincenzo Vitelli, Zev Bryant, Margaret L Gardel, et al. Spatiotemporal control of liquid crystal structure and dynamics through activity patterning. *Nature Materials*, 20(6):875–882, 2021.
[68]Tyler D Ross, Heun Jin Lee, Zijie Qu, Rachel A Banks, Rob Phillips, and Matt Thomson. Controlling organization and forces in active matter through optically defined boundaries. *Nature*, 572(7768):224–229, 2019.
[69]Maya Malik-Garbi, Niv Ierushalmi, Silvia Jansen, Enas Abu-Shah, Bruce L Goode, Alex Mogilner, and Kinneret Keren. Scaling behaviour in steady-state contracting actomyosin networks. *Nature physics*, 15(5):509–516, 2019.
[70]Geneviève Dupont, Martin Falcke, Vivien Kirk, and James Sneyd. *Models of Calcium Signalling*. Springer, 2016.
[71]Chien-Jung Lo. *Sodium energetics of chimeric flagellar motors in Escherichia coli*. PhD thesis, University of Oxford, 2007.
[72]Xiaobing Chen and Howard C Berg. Torque-speed relationship of the flagellar rotary motor of escherichia coli. *Biophysical Journal*, 78(2):1036–1041, 2000.
[73]Johannes Schindelin, Ignacio Arganda-Carreras, Erwin Frise, Verena Kaynig, Mark Longair, Tobias Pietzsch, Stephan Preibisch, Curtis Rueden, Stephan Saalfeld, Benjamin Schmid, et al. Fiji: an open-source platform for biological-image analysis. *Nature Methods*, 9(7):676–682, 2012.
[74]Tristan Ursell, Timothy K Lee, Daisuke Shiomi, Handuo Shi, Carolina Tropini, Russell D Monds, Alexandre Colavin, Gabriel Billings, Ilina Bhaya-Grossman, Michael Broxton, et al. Rapid, precise quantification of bacterial cellular dimensions across a genomic-scale knockout library. *BMC Biology*, 15(1):1–15, 2017.
[75]Ray Chang and Manu Prakash. Entangled architecture of rough endoplasmic reticulum (RER) and vacuoles enables topological damping in cytoplasm of an ultra-fast giant cell. *bioRxiv*, 2021.
[76]Stefan Schuster, Marko Marhl, and Thomas Höfer. Modelling of simple and complex calcium oscillations: From single-cell responses to

intercellular signalling. *European Journal of Biochemistry*, 269(5):1333–1355, 2002.

[77] Silvina Ponce Dawson, Joel Keizer, and John E Pearson. Fire–diffuse–fire model of dynamics of intracellular calcium waves. *Proceedings of the National Academy of Sciences*, 96(11):6060–6063, 1999.

[78] Joel Keizer, Gregory D Smith, Silvina Ponce-Dawson, and John E Pearson. Saltatory propagation of Ca^{2+} waves by Ca^{2+} sparks. *Biophysical Journal*, 75(2):595–600, 1998.